

## Journal Pre-proofs

Synthesis of novel LaCoO<sub>3</sub>/graphene catalysts as highly efficient peroxymonosulfate activator for the degradation of organic pollutants

Mohaned Hammad, Steven Angel, Ahmed K. Al-kamal, Anam Asghar, Amin Said Amin, Mena-Alexander Kräenbring, Haakon T. A. Wiedemann, Vineetha Vinayakumar, Md Yusuf Ali, Paolo Fortugno, Cheolyong Kim, Torsten C. Schmidt, Christopher W. M. Kay, Christof Schulz, Doris Segets, Hartmut Wiggers

PII: S1385-8947(22)05380-3  
DOI: <https://doi.org/10.1016/j.cej.2022.139900>  
Reference: CEJ 139900

To appear in: *Chemical Engineering Journal*

Received Date: 25 May 2022  
Revised Date: 4 October 2022  
Accepted Date: 15 October 2022

Please cite this article as: M. Hammad, S. Angel, A.K. Al-kamal, A. Asghar, A. Said Amin, M-A. Kräenbring, H. T. A. Wiedemann, V. Vinayakumar, M. Yusuf Ali, P. Fortugno, C. Kim, T.C. Schmidt, C. W. M. Kay, C. Schulz, D. Segets, H. Wiggers, Synthesis of novel LaCoO<sub>3</sub>/graphene catalysts as highly efficient peroxymonosulfate activator for the degradation of organic pollutants, *Chemical Engineering Journal* (2022), doi: <https://doi.org/10.1016/j.cej.2022.139900>

This is a PDF file of an article that has undergone enhancements after acceptance, such as the addition of a cover page and metadata, and formatting for readability, but it is not yet the definitive version of record. This version will undergo additional copyediting, typesetting and review before it is published in its final form, but we are providing this version to give early visibility of the article. Please note that, during the production process, errors may be discovered which could affect the content, and all legal disclaimers that apply to the journal pertain.

© 2022 Elsevier B.V. All rights reserved.



1 **Title page**2 **Synthesis of novel LaCoO<sub>3</sub>/graphene catalysts as highly efficient**  
3 **peroxymonosulfate activator for the degradation of organic pollutants**4 Mohaned Hammad<sup>a\*</sup>, Steven Angel<sup>c</sup>, Ahmed K. Al-kamal<sup>c,g</sup>, Anam Asghar<sup>b</sup>, Amin Said Amin<sup>a</sup>, Mena-  
5 Alexander Kräenbring<sup>a</sup>, Haakon T. A. Wiedemann<sup>d</sup>, Vineetha Vinayakumar<sup>a</sup>, Md Yusuf Ali<sup>c</sup>, Paolo  
6 Fortugno<sup>e</sup>, Cheolyong Kim<sup>b</sup>, Torsten C. Schmidt<sup>b</sup>, Christopher W. M. Kay<sup>d,f</sup>, Christof Schulz<sup>e,e</sup>, Doris  
7 Segets<sup>a,e\*</sup>, Hartmut Wiggers<sup>c,e\*</sup>8 <sup>a</sup> Institute for Combustion and Gas Dynamics – Particle Science and Technology (IVG-PST), University  
9 of Duisburg-Essen, Duisburg, Germany10 <sup>b</sup> Instrumental Analytical Chemistry and Centre for Water and Environmental Research, University of  
11 Duisburg-Essen, Essen, Germany12 <sup>c</sup> Institute for Combustion and Gas Dynamics – Reactive Fluids (IVG-RF), University of Duisburg-  
13 Essen, Duisburg, Germany14 <sup>d</sup> Department of Chemistry, Saarland University, Saarbrücken, Germany15 <sup>e</sup> Center for Nanointegration Duisburg-Essen (CENIDE), University of Duisburg-Essen, Duisburg,  
16 Germany17 <sup>f</sup> London Centre for Nanotechnology, University College London, 17-19 Gordon Street, London WC1H  
18 0AH, United Kingdom19 <sup>g</sup> Department of Materials Engineering, University of Al-Mustansiriyah, Baghdad, Iraq

20

21 Corresponding authors:

22 Dr. Mohaned Hammad\*

23 Prof. Doris Segets\*

24 Institute for Combustion and Gas Dynamics – Particle Science and Technology

- 25 Prof. Hartmut Wiggers\*
- 26 Institute for Combustion and Gas Dynamics – Reactive Fluids
- 27 University of Duisburg-Essen
- 28 Carl-Benz-Str. 199
- 29 47057 Duisburg, Germany
- 30 mohaned.hammad@uni-due.de
- 31 doris.segets@uni-due.de
- 32 hartmut.wiggers@uni-due.de

34 **Abstract**

35 Metal leaching in perovskite-based catalysts during peroxymonosulfate activation processes can  
36 severely restrict their application in wastewater treatment. Therefore, enhancing the stability of  
37 perovskite nanostructures is crucial to improve catalytic performance and broaden applications but has  
38 been rarely achieved so far. We developed a scalable method to synthesize novel stable and  
39 environmentally-friendly nanocomposites of LaCoO<sub>3</sub> and few-layer graphene (consisting of roughly  
40 nine layers) for the removal of organic pollutants from wastewater. With abundant oxygen vacancies  
41 and synergistic effects between LaCoO<sub>3</sub> (LCO) and few-layer graphene, the novel LaCoO<sub>3</sub>/graphene  
42 catalyst exhibits outstanding catalytic degradation (>99 %) of diclofenac, metoprolol, carbamazepine,  
43 and bisphenol A at a high concentration (40 mg/l) in less than 10 minutes in the peroxymonosulfate  
44 activation system, with mineralization of 57, 55, 61, and 62 %, respectively. The LaCoO<sub>3</sub>/graphene  
45 catalyst exhibited excellent reusability and high catalytic performance within a wide pH range (3–11).  
46 The formation of LaCoO<sub>3</sub>/graphene composites prevents cobalt leaching (0.004 mg/l), stabilizes sub-  
47 stoichiometric LCO and thus increases the content of Co<sup>2+</sup> in the structure, leading to much higher  
48 catalytic activity than that of pure LaCoO<sub>3</sub>. Electron paramagnetic resonance and radical quenching  
49 experiments revealed that both radical pathways (SO<sub>4</sub><sup>•-</sup>, •OH, and O<sub>2</sub><sup>•-</sup>) and non-radical pathways (<sup>1</sup>O<sub>2</sub>)  
50 contribute to bisphenol A degradation and the relative contributions of •OH, SO<sub>4</sub><sup>•-</sup>, and <sup>1</sup>O<sub>2</sub>/O<sub>2</sub><sup>•-</sup> were  
51 determined to 13.4, 32.6, and 54 % for BPA removal, respectively. Overall, our results indicate that  
52 LaCoO<sub>3</sub>/graphene is a promising material towards peroxymonosulfate activation for environmental  
53 remediation.

54 **Keywords:** Bisphenol A, gas-phase synthesis, graphene, heterogeneous catalysis, peroxymonosulfate.

55

56

57

## 58 1 Introduction

59 Trace organic pollutants such as industrial chemicals and personal care and pharmaceutical products  
60 discharged into the environment have brought serious threats to nature and humans due to their  
61 persistence, toxicity, and bioaccumulation [1,2]. Advanced oxidation processes (AOPs) are considered  
62 a promising technology to degrade organic pollutants [3]. The Fenton reaction is a classical AOP method  
63 that utilizes iron ions/salts to activate hydrogen peroxide ( $\text{H}_2\text{O}_2$ ) and produce hydroxyl radicals ( $\cdot\text{OH}$ ,  
64 oxidative potential 1.9–2.7 V) at acidic pH (2.5–3.5) [4]. However, the traditional Fenton reaction is  
65 inherently limited by the narrow range of the working pH, metal leaching, and sludge generation during  
66  $\text{H}_2\text{O}_2$  activation [5]. In the last decade, sulfate radical-based advanced oxidation processes (SR-AOPs)  
67 were developed as promising alternatives to the classical Fenton reaction because of their high oxidative  
68 potential (2.5–3.1 V), wide pH adaptability (2–9), and long half-life time (30–40 ms) [6]. In order to  
69 generate sulfate radicals, peroxymonosulfate (PMS), or peroxydisulfate (PDS) are used most frequently  
70 and activated by heat [7], UV or visible light [8], microwave ultrasound [9], electrochemical processes  
71 [10], and transition metal ions (e.g., Co, Mn, Cu, and Fe) [11]. In this regard, different transition metal  
72 oxide catalysts such as  $\text{Co}_3\text{O}_4$ ,  $\text{CuFe}_2\text{O}_4$ ,  $\text{LaCoO}_3$ , etc. [12–14], zero-valent metal [15], and carbon-based  
73 materials [16] are reported to activate peroxymonosulfate (PMS) or peroxydisulfate (PDS) in refractory  
74 chemical degradation processes. Among them, transition metal-based perovskites such as  $\text{LaCoO}_3$   
75 (LCO) nanoparticles have received considerable attention in PMS activation because of their structural  
76 flexibility, high electronic conductivity, and their ability to create oxygen vacancies [17,18]. Our recent  
77 study reveals that the catalytic activity of  $\text{LaCoO}_3$  nanomaterials is significantly higher than that of  
78  $\text{Co}_3\text{O}_4$  nanoparticles towards PMS activation for bisphenol A degradation [19]. Furthermore, a previous  
79 report shows also that the cobalt-based perovskite,  $\text{Ba}_{0.5}\text{Sr}_{0.5}\text{Co}_{0.8}\text{Fe}_{0.2}\text{O}_{3-\delta}$ , exhibited better redox  
80 potential and electrical conductivity than  $\text{Co}_3\text{O}_4$  nanoparticles for PMS activation [20].  $\text{LaCoO}_3$  has been  
81 widely used as catalyst in the field of water and ethanol oxidation [21], cyclohexene oxidation [22],  
82 catalytic combustion [23], photocatalysis [24], and heterogeneous Fenton reactions [25]. However, the  
83 reusability and toxicity of cobalt-based perovskite due to cobalt leaching in aqueous systems severely  
84 impeded their practical application in wastewater treatment. Therefore, fabricating stable and

85 environmentally-friendly cobalt-based solid-state catalysts has attracted increasing interest for PMS  
86 activation.

87 For the synthesis of perovskites, various methods have been explored. These methods are usually  
88 grouped into different categories [26,27]. One category is known as solid–solid synthesis, including  
89 methods such as microwave, combustion, ceramic, and mechanochemistry synthesis. As these methods  
90 are usually followed by extended high-temperature calcination to reach the desired crystallographic  
91 phase, the final particles typically provide low specific surface areas – with few exceptions (e.g.,  
92 activated reactive synthesis [28]). In the quest of phase-pure perovskites with high specific surface areas,  
93 liquid-based or solution-mediated synthesis has been also explored. This category includes methods  
94 such as sol-gel or Pechini processes, or nanocasting (e.g., using soft or hard templates). Nevertheless,  
95 these methods are also associated with high-temperature calcination and the resulting lack of  
96 morphology control [29] (e.g., in sol-gel or Pechini methods) or with the complex removal of templates  
97 (e.g., silica in nanocasting methods) and low yields of material [26]. In contrast to these conventional  
98 synthesis routes, spray-flame synthesis of perovskites is a method that enables production of phase-pure  
99 and high specific surface area materials in a single step [30,31]. Furthermore, this method allows the  
100 use of low-cost precursors (e.g., metal nitrates or chlorides) and facilitates the synthesis of high-quality  
101 perovskites in a continuous and scalable way [32].

102 Recently, researchers have attempted to improve the catalytic activity and stability of catalysts by  
103 incorporating catalysts on carbonaceous materials such as carbon [33],  $C_3N_4$  [34], carbon quantum dots  
104 [35], and graphene derivatives [36]. Comparing with the above mentioned carbonaceous materials,  
105 single and few-layer graphene provides high electrochemical stability and high surface area that can be  
106 used as adsorbent support for the decomposition of organic pollutants [37]. Xu et al. reported that  
107 graphene revealed an improved adsorption capacity for bisphenol A (82 mg/g at 302.15 K) compared to  
108 other carbonaceous materials [38]. Due to their high electron mobility and unique optical properties,  
109 graphene/semiconductor nanoparticles-based composites have also shown to possess a high  
110 photocatalytic activity [39–41]. As reported in one of our previous works, the high surface area of few-  
111 layer graphene and the presence of unpaired  $\pi$  electrons in the graphene structure facilitate a fast

112 transport of the photo-induced electrons between graphene and  $\text{Fe}_3\text{O}_4$  [42], which improves the  
113 degradation efficiency towards methylene blue. Besides, graphene exhibits exciting properties such as  
114 mechanical flexibility, chemical stability, and optical transparency [43]. For instance, Wang et al.  
115 demonstrated that the catalytic activity of a  $\text{Co}_3\text{O}_4$ /graphene hybrid in terms of Orange II degradation  
116 was 2.5 times faster compared to that of pure  $\text{Co}_3\text{O}_4$ . Graphene facilitates the electric conductivity of the  
117 composite compared to pure  $\text{Co}_3\text{O}_4$ , and therefore promotes electron transfer between the catalyst and  
118 PMS, resulting in increased sulfate radical ( $\text{SO}_4^{\cdot-}$ ) generation [44]. However, to the best of our  
119 knowledge, there is no report on the application of  $\text{LaCoO}_3$ /graphene (LCO/Gr) in PMS activation. This  
120 motivates the development of a new strategy for scalable production of LCO/Gr nanostructures for PMS  
121 activation. Usually, the incorporation of cobalt-based catalysts in graphene is achieved by hydrothermal  
122 [45] or post-impregnating methods [46], which requires additional steps for surface functionalization of  
123 nanoparticles and/or graphene-based structures and needs a subsequent chemical reaction step to reduce  
124 graphene oxide [47,48]. The hybrids of cobalt-based nanoparticles and graphene can always show low  
125 metal leaching [49]. However, the better chemical stability was not based on the low cobalt leaching  
126 [50]. In fact, no metal leaching was observed in some metal-free catalysts, but they showed poor  
127 chemical stability after PMS activation [51].

128 The aim of this study is to prepare a stable composite of LCO and few-layer graphene (hereafter referred  
129 to as graphene for simplicity), to investigate the contribution of  $\text{LaCoO}_3$  and graphene and in particular  
130 their interaction with respect to the degradation of pollutants, to understand the physicochemical  
131 properties of the novel  $\text{LaCoO}_3$ /graphene catalyst, and to propose an activation mechanism for  
132 peroxymonosulfate. We demonstrate a convenient and scalable method to prepare stable LCO/Gr  
133 nanocomposites. LCO nanoparticles synthesized via spray-flame synthesis are bonded to graphene from  
134 scalable microwave-plasma synthesis by a simple ultrasonication technique. This approach follows our  
135 previous studies showing that the binding of graphene (30 % w/w) to nanoparticles hinders nanoparticle  
136 agglomeration as well as restacking of the graphene sheets [42].

## 137 2 Materials and methods

### 138 2.1 Materials

139 For the synthesis of LCO,  $\text{La}(\text{NO}_3)_3 \cdot 6 \text{H}_2\text{O}$  (AppliChem Panreac, > 99.0 % purity) and  $\text{Co}(\text{NO}_3)_2 \cdot 6 \text{H}_2\text{O}$   
140 (Honeywell, > 99.0 % purity) were used as precursors dissolved in a mixture of ethanol (VWR, > 99.9 %  
141 purity) and 2-ethylhexanoic acid (2-EHA) (Alfa Aesar, >99 % purity). 5,5-dimethyl-1-pyrroline  
142 N-oxide (> 97.0 %; TCI), 2,2,6,6-tetramethyl-4-piperidon ( $\geq 95$  %), bisphenol A ( $\geq 99$  %), diclofenac  
143 sodium salt ( $\geq 98$  %), metoprolol tartrate salt ( $\geq 98$  %), carbamazepine ( $\geq 98$  %), potassium  
144 peroxymonosulfate (100 %), sodium phosphate monobasic ( $\geq 99$  %), sodium nitrate ( $\geq 99$  %), sodium  
145 chloride ( $\geq 99$  %), sodium hydrogencarbonate ( $\geq 99$  %),  $\beta$ -carotene ( $\geq 95$  %), tert-butyl alcohol  
146 ( $\geq 99.5$  %), *p*-benzoquinone ( $\geq 98$  %), potassium bicarbonate ( $\geq 99.5$  %), and potassium iodide  
147 ( $\geq 90$  %) were purchased from Sigma Aldrich for the catalysis tests. Sodium hydroxide ( $\geq 97$  %) and  
148 nitric acid (> 69 %, both VWR chemical) were used to adjust the pH of the respective solution. All  
149 chemicals were used as received without further purification. All gases (argon (Ar), oxygen ( $\text{O}_2$ ),  
150 methane ( $\text{CH}_4$ ), hydrogen ( $\text{H}_2$ ), and nitrogen ( $\text{N}_2$ )) were supplied from Air Liquide with a purity of  
151 99.5 % or higher. Upper Mississippi River NOM (NOM, 1R110N) was received from International  
152 Humic Substances Society (IHSS, Saint Paul, MN, USA) as dry solid extract. NOM stock solutions  
153 were prepared by mixing the required concentration of NOM in 50 ml of distilled water containing 0.1  
154 mol/l NaOH with shaking overnight. Afterwards, the solutions were filtered through a polypropylene  
155 syringe filter (0.22  $\mu\text{m}$ ) and the pH was adjusted to 7 using  $\text{H}_3\text{PO}_4$ .

### 156 2.2 Synthesis of LCO nanoparticles

157 The synthesis of LCO nanoparticles was performed using an enclosed spray-flame reactor – described  
158 previously [31,52] using the standardized *SpraySyn* burner [53]. For the preparation of the precursor  
159 solutions,  $\text{La}(\text{NO}_3)_3 \cdot 6 \text{H}_2\text{O}$  and  $\text{Co}(\text{NO}_3)_2 \cdot 6 \text{H}_2\text{O}$  in a total concentration of 0.2 mol/l were dissolved in  
160 a mixture of ethanol (35 Vol.%) and 2-EHA (65 Vol.%). By using a syringe pump, the precursor solution  
161 was supplied to the reactor at a constant flow rate of 2 ml/min via a capillary surrounded by an annular



162 gap through which O<sub>2</sub> was supplied at a flow rate of 10 slm as dispersion gas. The atomization of the  
163 solution was done by the shear forces caused by the contact of the high velocity dispersion gas with the  
164 solution at the capillary tip. The resulting aerosol was ignited by a premixed flat pilot flame (3 slm CH<sub>4</sub>  
165 and 20 slm O<sub>2</sub>, stabilized on a sintered bronze plate), coaxially surrounding the spray nozzle. The spray  
166 flame was shielded from the reactor walls by a surrounding sheath-gas (140 slm, compressed air). To  
167 control the temperature of the off-gas and to minimize the sintering of the nanoparticles, an additional  
168 quench gas flow – 200 slm compressed air – was supplied downstream of the spray flame. The pressure  
169 in the reaction chamber was held constant at 970 mbar and the nanoparticles were collected from the  
170 reactor off-gas using a membrane filter.

### 171 **2.3 Synthesis of graphene**

172 The synthesis of freestanding few-layer graphene flakes was carried out using a microwave plasma  
173 reactor as described before [54]. A microwave antenna (iplas company) was used to focus the  
174 microwaves to the center of a quartz tube located in the center of the antenna. Ar (30 slm) and H<sub>2</sub> (1 slm)  
175 were used as plasma gases and to stabilize the centrally introduced precursor gas flow. The plasma was  
176 ignited using a 2-kW microwave generator (Muegge, Germany) that operates at a frequency of 2.45  
177 GHz. Ethanol (0.5 ml/min) used as graphene precursor was vaporized at 180 °C and mixed with argon  
178 as carrier gas (5 slm) using a controlled evaporation mixing system (CEM W-209-333-P, Bronkhorst).  
179 The mixture was fed through a nozzle into the center of the plasma zone. The resulting graphene flakes  
180 were collected from a PTFE-coated filter membrane located downstream the reaction zone. The typical  
181 production rate of this process is 200 mg/h.

182 In order to disperse graphene in water and to support the self-assembly with LCO nanoparticles, the  
183 graphene surface had to be modified with carboxyl groups. Thus, pristine graphene was stirred in a  
184 concentrated mixture of sulfuric and nitric acid (3:1) for a few minutes, collected by centrifugation  
185 (12,000 rpm), and washed with de-ionized water for three times. The carboxylated graphene was then  
186 dried at 60 °C under vacuum for 24 hours.

## 187 **2.4 Reproducible fabrication of LCO/Gr**

188 LaCoO<sub>3</sub>/graphene nanocomposites were prepared via a controllable ultrasonication-assisted self-  
189 assembly process. The LCO/Gr nanocomposites were assembled through an electrostatic interaction  
190 between the positively charged LCO (+37.4 mV, pH=9) and the negatively charged graphene (-40.6  
191 mV, pH=9). 300 mg carboxylated graphene were dispersed in 60 ml water by sonication (Hielscher  
192 UP200S, 60 % amplitude, 60 % cycle duty (0.6 s pulse rate)) for 30 minutes. Subsequently, dispersions  
193 of LCO (700 mg particles in 100 ml water by sonication) were added to the graphene dispersion under  
194 stirring and the obtained mixtures were further sonicated for another 60 minutes on an ice bath. The  
195 final pH of the suspension was 9. The product was collected via centrifugation and dried at 60 °C under  
196 vacuum for 24 hours.

## 197 **2.5 Materials characterization**

198 Characterization by thermal gravimetric analysis (TGA) was performed with a Netzsch 449 F1 Jupiter  
199 at temperatures increasing from room temperature to 1000 °C with a heating rate of 10 K/min under the  
200 flow of synthetic air (250 ml/min). X-ray diffraction (XRD) patterns were recorded in the  $2\theta$  range of  
201 10–80° using a PANalytical X'Pert X-ray diffractometer equipped with a Cu K<sub>α</sub> radiation  
202 ( $\lambda = 1.5406 \text{ \AA}$ ). The morphology of the synthesized nanoparticles was acquired with a JEOL  
203 JEM-2200FS transmission electron microscope (TEM). Raman spectra were collected using a Renishaw  
204 inVia Raman microscope with excitation laser wavelengths of 532 nm (1000–1800 cm<sup>-1</sup>) and 680 nm  
205 (100–1000 cm<sup>-1</sup>). The surface composition of the materials was studied by X-ray photoelectron  
206 spectroscopy (XPS) using a VersaProbe II (Ulvac-Phi) with monochromatic Al K<sub>α</sub> light at an emission  
207 angle of 45°. The specific surface area was analyzed by the Brunauer-Emmett-Teller (BET) method  
208 with a Quantachrome NOVA2200 analyzer. The pH point of zero charge (pH<sub>pzc</sub>) of the catalysts'  
209 dispersion was determined by a Malvern Zetasizer. In order to evaluate the electrochemical behavior of  
210 the catalyst, electrochemical impedance spectroscopy (EIS) was performed using a Solartron 1260 in  
211 the frequency range between 0.1 Hz and 1 MHz at an applied AC potential value of 100 mV. To that  
212 end, the catalyst powder samples were pressed into pellets (thickness between 0.3 and 0.5 mm) by a 5-

213 mm stainless steel die (force: 15 kN, for 15–30 minutes). Then, the pellets were coated with gold on  
214 both sides to improve the contact between the platinum electrodes (size 5 mm). The Hansen solubility  
215 (understood here in the context of similarity) parameter (HSP) were determined according to a method  
216 reported by Bapat et al. using analytical centrifugation (AC) [55]. Briefly, 1 wt/v% LCO and LCO/Gr  
217 dispersions were prepared by 5 minutes sonication of the powder in the respective probe liquids listed  
218 in Table S1. The dispersions were filled into cells and then inserted into the rotor and centrifuged at  
219 2000 rpm for 20 hours. AC measurements were performed using a LUMiSizer LS 651 (LUM GmbH,  
220 Berlin, Germany) with a wavelength of 410 nm. Reactive radicals spectra were obtained using an  
221 electron-spin resonance spectrometer (MiniScope MS-5000, Freiberg Instruments, Germany) and  
222 recorded using a microwave power of 10 mW and a modulation amplitude of 0.2 G at room temperature.  
223 A mercury intrusion porosimeter (PoreMaster-60, Anton Paar) was used to determine the porosity and  
224 pore size distribution. The pore radius ( $r$ ) was determined using the Washburn equation.

$$P = \frac{-2\gamma \cos\theta}{r} \quad (\text{Equation 1})$$

226 Where  $P$  is the pressure  $\gamma$  is the interfacial energy (surface tension) of mercury and  $\theta$  is the contact angle  
227 of mercury with the material. The mercury is intruded into the sample at a rate of 7–28 MPa/min and  
228 the pressure ranged from 100 Pa to 400 MPa.

## 229 2.6 Catalysis studies and analyses

230 The degradation performance of the as-prepared LCO catalyst was evaluated for BPA degradation. In a  
231 typical run, 6 mg catalyst was initially dispersed into 60 ml BPA aqueous solution (40 mg/l) at 25 °C,  
232 and the initial pH was adjusted by H<sub>2</sub>SO<sub>4</sub> and NaOH to different pH values (3–11). The resulting  
233 suspension was continuously stirred for 30 min to ensure the establishment of an adsorption/desorption  
234 equilibrium between BPA molecules and the as-prepared catalyst before a certain amount of PMS was  
235 added. During the experiment, 2 ml of the suspension was withdrawn at given time intervals,  
236 immediately quenched with 0.5 ml methanol, centrifuged (12,000 rpm, 20 min) to remove the particles,  
237 and the supernatant was injected into a HPLC vial. To evaluate the reusability of the catalyst, the as-

238 prepared nanoparticles were recovered by a centrifuge (12,000 rpm, 20 min), washed with de-ionized  
239 water three times, and then re-dispersed into 60 mL BPA aqueous solution for the next use.

240 Moreover, degradation of DCF, MTP, and CBZ was also investigated to test the catalytic activity of the  
241 as-prepared catalyst. To obtain the degradation reaction kinetics of organic pollutants, pseudo-first-order  
242 kinetics reaction rate constants ( $k_{app}$ ) were determined according to the following equation:

$$243 \quad \ln \left( \frac{C_t}{C_0} \right) = -k_{app}t \quad (\text{Equation 2})$$

244 Where  $C_t$  depicts the pollutant concentration at time  $t$ ,  $C_0$  is the initial pollutant concentration, and  $k_{app}$   
245 is the reaction rate constant.

246 The concentrations of BPA, DCF, MTP, and CBZ were analyzed by high-performance liquid  
247 chromatography (HPLC, Shimadzu LC-10AT) with an EVO C18 column (Kinetex 5 $\mu$ m EVO C18 100  
248 Å 100  $\times$  3.0 mm, Phenomenex). The flow rate of the mobile phase consisting of 0.1 % formic acid in  
249 water and methanol (60:40, v:v) was 0.5 ml/min. To determine the residual concentration of PMS,  
250 100  $\mu$ l of the suspension was withdrawn at given time intervals, mixed with potassium bicarbonate  
251 (5 g/l) and potassium iodide (40 g/l), and then analyzed by UV-Vis spectroscopy (Varian Cary 400) at  
252 a wavelength of 352 nm [56]. The mineralization rate was determined using a total organic carbon  
253 analyzer (TOC-5000A, Shimadzu). The effects of pH, temperature, and co-existing ions (such as  $\text{Cl}^-$ ,  
254  $\text{NO}_3^-$ ,  $\text{H}_2\text{PO}_4^-$ ,  $\text{HCO}_3^-$ , etc.) on the PMS activation of LCO/Gr composite catalyst were also investigated.  
255 To evaluate the reusability of the LCO/Gr nanoparticles, the LCO/Gr catalysts were collected by  
256 centrifugation (Sigma 3-30KS centrifuge, Sigma Laborzentrifugen GmbH, Germany) at 14,000 rpm for  
257 10 min, followed by thorough washing with deionized water and re-dispersion into fresh BPA solution  
258 for the next experimental run. To identify the dominant reactive radicals in the system, ethanol (EtOH),  
259 tert-butyl alcohol (TBA), and  $\beta$ -carotene were used as scavengers for  $\text{SO}_4^{\cdot-}$  and  $\cdot\text{OH}$ ,  $\cdot\text{OH}$ , and  $^1\text{O}_2$   
260 respectively. Furthermore, electron paramagnetic resonance experiments were performed to identify  
261  $\text{SO}_4^{\cdot-}$  and  $\cdot\text{OH}$ , and  $^1\text{O}_2$ , respectively, using 5,5-dimethyl-1-pyrroline N-oxide (DMPO) and 2,2,6,6-  
262 tetramethyl-4-piperidon (TEMP) as spin traps. The EPR spectra were measured using a MiniScope MS-  
263 5000 electron spin resonance spectrometer (modulation amplitude 0.2 G, microwave power, 10 mW).

264 The concentration of dissolved metal ions was determined by atomic absorption spectroscopy (AAS,  
265 Thermo Electron Corporation, M-Serie).

### 266 **3 Results and discussion**

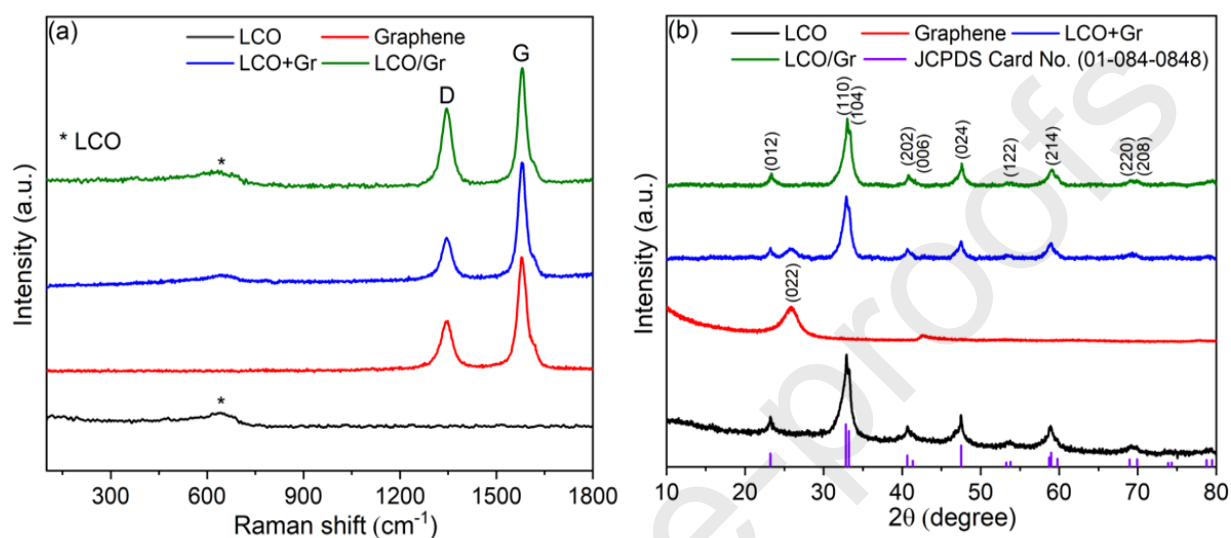
#### 267 **3.1 Preparation of LCO/Gr nanocomposites**

268 To quantify the amount of adsorbates and carbon in as-synthesized LCO and the LCO/Gr  
269 nanocomposites, TGA measurements were performed at up to 1000 °C under synthetic air to decompose  
270 residuals on the particle surface as well as graphene (see supplementary material, Figure S1). The weight  
271 loss of the pristine LCO is about 19 % and can be ascribed to the loss of adsorbates such as water (3 %,  
272 50–170 °C) and the oxidation of unburned combustion residuals (16 %, 200–600 °C) releasing water  
273 and CO<sub>2</sub>. Compared to the result of as-synthesized LCO, the additional weight loss for LCO/Gr is 32 %,  
274 which can be attributed to the oxidation of graphene (300–750 °C). Accordingly, the observed graphene  
275 weight loss value is in good agreement with the intended composition of the LCO/Gr nanocomposite.

#### 276 **3.2 Structural characterization of LCO/Gr nanocomposites**

277 Raman spectroscopy was employed as a qualitative method to evaluate the purity of the synthesized  
278 graphene and to identify the phase composition of the LCO and LCO/Gr nanoparticles (Figure 1a). The  
279 peak at around 650 cm<sup>-1</sup> measured for LCO (black graph) matches the Co–O stretching vibration of the  
280 LaCoO<sub>3</sub> phase [57], whereas the Raman spectrum of graphene (red graph) consists of two peaks. The D  
281 (1350 cm<sup>-1</sup>) and G (1580 cm<sup>-1</sup>) bands are ascribed to sp<sup>3</sup> defects and the first-order scattering of sp<sup>2</sup>  
282 carbon atom domains in a 2D hexagonal carbon lattice, respectively. The intensity ratio between the D  
283 and G bands ( $I_D/I_G$ ) is a measure of the degree of disorder and defects in the graphene structure [58].  
284 The observed  $I_D/I_G$  ratio of 0.5 is quite low, indicating a very high quality of the as-synthesized few-  
285 layer graphene (see supplementary material, Figure S3a) with a low degree of structural defects.  
286 Importantly, there is a significant difference in  $I_D/I_G$  values between the pure few-layer graphene and  
287 LCO/Gr composite (0.79, green graph in Figure 1a). However, when LCO (0.68 g) and graphene

288 (0.32 g) were mixed without having been processed to the LCO/Gr nanocomposite in advance, there is  
 289 almost no change in  $I_D/I_G$  (0.54, blue graph). This provides strong evidence that the deposition of LCO  
 290 nanoparticles on the graphene nanosheets did introduce defects in the graphene structure due to strong  
 291 interaction between LCO nanoparticles and graphene sheets.



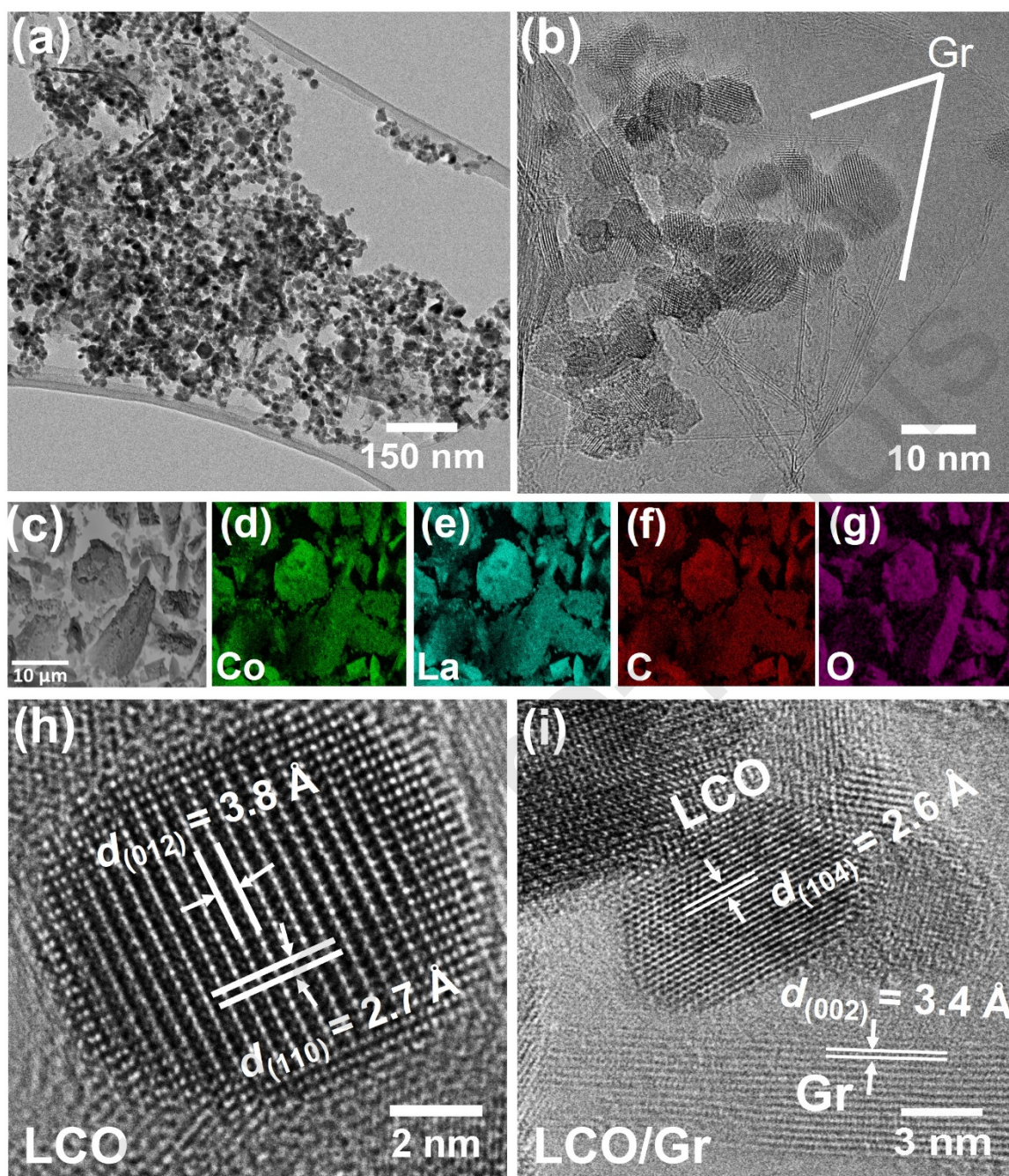
292  
 293 Figure 1. a) Raman spectra and b) XRD patterns for LCO, graphene, LCO+Gr, and LCO/Gr nanopowders. All  
 294 Raman spectra were measured with an excitation wavelength of 532 nm (1000–1800  $\text{cm}^{-1}$ ) and 680 nm (100–  
 295 1000  $\text{cm}^{-1}$ ).

296 The crystal structure of LCO, graphene, and LCO/Gr materials was characterized by powder XRD  
 297 (Figure 1b). The LCO diffraction peaks (black graph) can be indexed to the rhombohedral  $\text{LaCoO}_3$   
 298 perovskite phase (JCPDS Card No. 01-084-0848) [59] and the peak shape is characteristic for  
 299 nanoparticles with high crystallinity. The mean crystallite sizes calculated from the XRD pattern of LCO  
 300 and LCO/Gr nanoparticles using Rietveld refinement are 9 and 9.3 nm, respectively (see supplementary  
 301 material, Figure S2), which is within the accuracy of the analysis and confirms that the LCO crystallites  
 302 do not change in structure and size. However, the lattice constants of LCO derived from Rietveld  
 303 refinement slightly increase with the introduction of LCO to graphene, whereas in case of the physical  
 304 mixture (LCO+Gr), there is no significant change (see supplementary material, Table S1). We interpret  
 305 this as a clear indication of chemical interaction between LCO and graphene in the composite material.  
 306 The weak expansion in the lattice constant of LCO in LCO/Gr (compared to bulk LCO and pristine LCO

307 nanoparticles) can be attributed to the presence of oxygen vacancies as also reported in literature [60,61].  
308 The intense and broad peak of graphene at  $2\theta = 26.2^\circ$  corresponds to the (002) plane of graphene.  
309 Interestingly, the characteristic (002) diffraction peak of graphene has almost disappeared in the LCO/Gr  
310 nanocomposite compared to the LCO+Gr nanoparticles mixture. This suggests that reduced graphene  
311 stacking occurs, most probably due to the coverage of graphene with LCO nanoparticles [44].

312 The morphology and chemical composition of LCO nanoparticles and LCO/Gr nanocomposites were  
313 characterized by TEM and elemental mapping. The sphere-like LCO nanoparticles (mean diameter  
314 about 7 nm, see supplementary material, Figure S3b) are uniformly distributed, covering almost the  
315 entire surface of the graphene sheets in LCO/Gr nanocomposite (Figure 2a). The high-magnification  
316 TEM image (Figure 2b) reveals that all LCO nanoparticles are connected to graphene. The chemical  
317 homogeneity of the LCO was evidenced by SEM energy-dispersive X-ray elemental mapping of  
318 LCO/Gr (Figure 2c–g). The EDX analysis was performed to further confirm the composition of the  
319 LCO/Gr material and showed that the La/Co ratio is about unity (see supplementary material, Figure  
320 S3e). Moreover, the high-resolution TEM (HRTEM) image of LCO/Gr further shows the crystal lattice  
321 fringes with an interlayer spacing of 0.26 and 0.34 nm, corresponding to the (104) and (002) planes of  
322 the rhombohedral  $\text{LaCoO}_3$  perovskite phase and highly crystalline graphene, respectively. This result is  
323 consistent with the XRD analysis.





324  
 325 Figure 2. a) Low-magnification, b) high-magnification TEM image, c–g) SEM image of LCO/Gr composites and  
 326 the corresponding elemental mapping of cobalt, lanthanum, carbon, and oxygen, and h–i) HRTEM image of  
 327 LCO and LCO/Gr particles.

328 The findings regarding LCO particle size and formation of few-layer graphene are further supported by  
 329 the results of nitrogen sorption. The mean particle diameter can be calculated from the results with the  
 330 following formula:

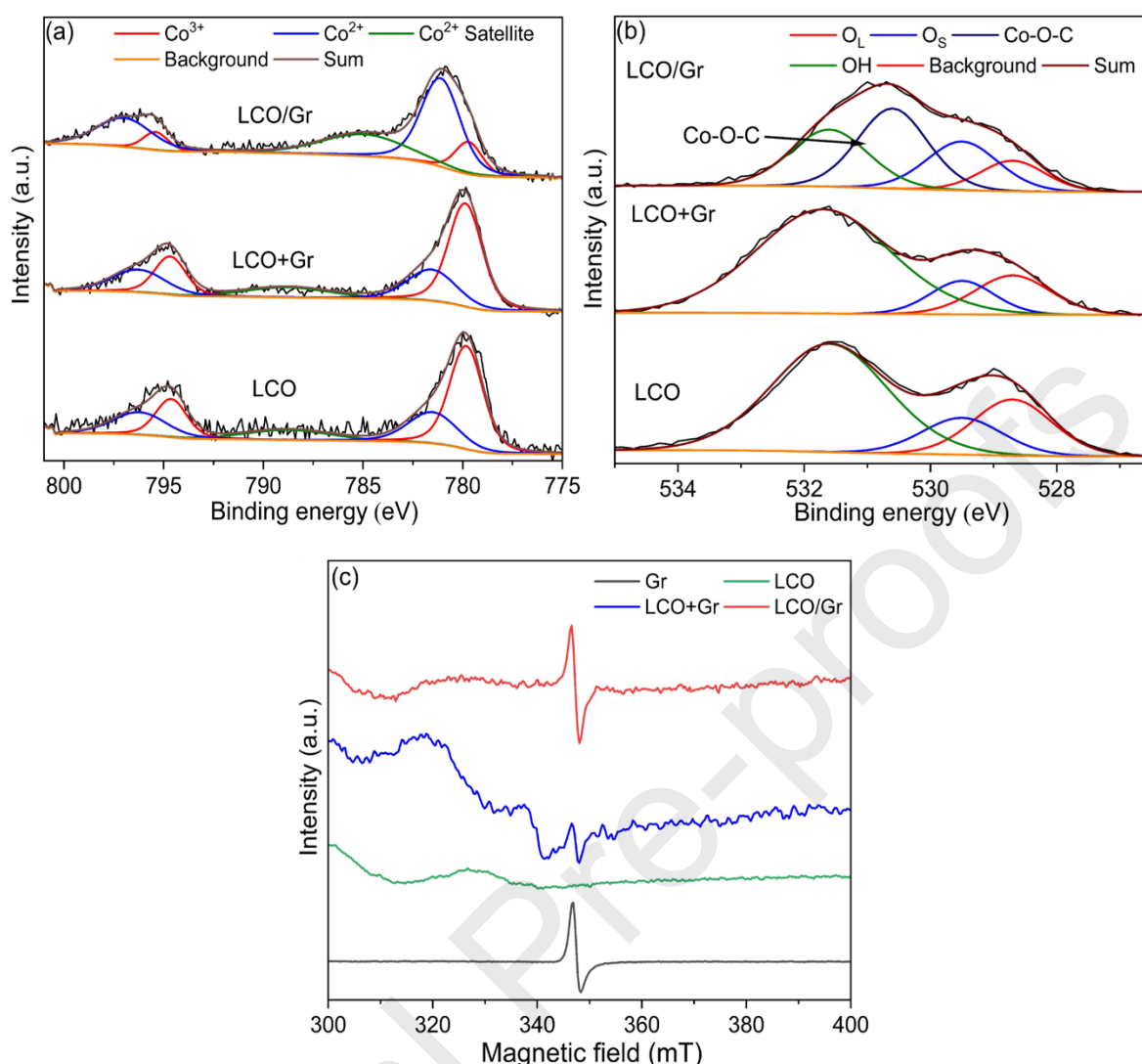


$$331 \quad \text{SSA} = \frac{6}{\rho d_p} \quad (\text{Equation 3})$$

332 where SSA is the specific surface area ( $\text{m}^2/\text{g}$ ),  $d_p$  stands for the particle diameter (nm), and  $\rho$  is the  
333 density of the analyzed materials system ( $\text{g}/\text{cm}^3$ ). Assuming spherical and non-aggregated particles,  
334 average particle sizes of 8.8 nm were derived from the measured BET surface areas of  $94 \text{ m}^2/\text{g}$ , using a  
335 LCO density of  $7.25 \text{ g}/\text{cm}^3$ . The average layer number of graphene can be estimated from the SSA of  
336 single-layer graphene ( $2630 \text{ m}^2/\text{g}$ ) versus the measured SSA of graphene. The SSA of graphene was  
337 measured as  $300 \text{ m}^2/\text{g}$  and suggests the formation of few-layer graphene with a mean number of  
338 nine graphene sheets stacked on top of each other. As expected, the SSA of the LCO/Gr composite was  
339 in between and was determined to be  $154 \text{ m}^2/\text{g}$ . Moreover, the pore-size distribution curve of LCO/Gr  
340 composite determined by the Washburn equation showed that the pore-size distribution is broad with 65  
341 % of the volume accounting for pores in the 2–3 nm range and 35 % are in the 6–12 nm range (see  
342 supplementary material, Figure S4). The mesoporous nature of LCO/Gr with high surface area suggests  
343 the presence of abundant active sites, which can activate PMS rapidly due to low mass transport  
344 resistance [62].

345 To confirm the surface interaction between LCO nanoparticles and graphene, XPS and FTIR  
346 spectroscopy was further studied. The surface chemical composition of LCO and LCO/Gr materials was  
347 investigated by XPS analysis (Figure 3a–b and Figure S5). Figure S5a shows the full surface XPS  
348 spectra of all samples. The four characteristic peak areas located at binding energies around 285, 530,  
349 779, and 835 eV belong to C1s, O1s, Co2p, and La3d, respectively. In the surface La3d high-resolution  
350 XPS spectra (see supplementary material, Figure S3d), the spectrum was fitted by peaks at 834 eV and  
351 851.5 eV for  $\text{La}3d_{5/2}$  and  $\text{La}3d_{3/2}$ , respectively, and their corresponding satellite peaks around 837.9 eV  
352 and 855.1 eV, which is assigned to  $\text{La}^{3+}$  ions in perovskite structures [63]. Besides, compared to LCO,  
353 the La3d peaks of the  $\text{LaCoO}_3/\text{graphene}$  was slightly shifted to a higher binding energy, which can be  
354 attributed to the interaction between  $\text{LaCoO}_3$  and graphene [64]. The surface Co2p XPS spectrum of  
355 LCO material was fitted by peaks at 779.7 and 794.5 eV. These are assigned to the  $\text{Co}2p_{3/2}$  and  $\text{Co}2p_{1/2}$   
356 spin-orbital peaks of  $\text{LaCoO}_3$  [65]. The energy difference of the doublet is about 15.2–15.3 eV, which  
357 is characteristic for the mixed oxide  $\text{LaCoO}_3$  structure [66]. Besides, small  $\text{Co}2p_{3/2}$  satellite peaks

358 positioned between 785–790 eV indicate the presence of a mixed oxidation state of  $\text{Co}^{3+}$  and  $\text{Co}^{2+}$   
359 surface ions. Upon mixing LCO and graphene (LCO+Gr), we could not observe any significant change  
360 in the intensity of the satellite peak and the peak position of  $\text{Co}2\text{p}_{3/2}$  and  $\text{Co}2\text{p}_{1/2}$ . However, compared to  
361 LCO+Gr, the surface  $\text{Co}2\text{p}$  XPS spectrum of the LCO/Gr material exhibits peaks at 780.5 eV and 796.4  
362 eV corresponding to the  $\text{Co}2\text{p}_{3/2}$  and  $\text{Co}2\text{p}_{1/2}$  states [67]. The increased intensity of the satellite peak  
363 around 785 eV along with the shifted peak position of  $\text{Co}2\text{p}_{3/2}$  and  $\text{Co}2\text{p}_{1/2}$  indicates that a part of the  
364  $\text{Co}^{3+}$  ions was converted to  $\text{Co}^{2+}$  and formed oxygen vacancies ( $\text{O}_{\text{vac}}$ ). In order to evaluate the surface  
365  $\text{O}_{\text{vac}}$  in both LCO and LCO/Gr samples, surface  $\text{O}1\text{s}$  spectra were deconvoluted into three major peaks  
366 centered at 528.7, 529.5, and 531.6 eV. This corresponds to surface lattice oxygen ( $\text{O}_{\text{L}}$ ), adsorbed  
367 oxygen species on the surface vacancy ( $\text{O}_{\text{S}}$ ), and surface hydroxyl groups (OH), respectively (Figure  
368 3b) [68]. The relative concentration of surface  $\text{O}_{\text{vac}}$  in the LCO/Gr sample was determined to be 23 %,  
369 which is higher compared to LCO nanoparticles (15 %) and LCO+Gr (14 %) and confirms the reduced  
370 oxidation of cobalt ions in the LCO/Gr sample, further manifesting the formation of  $\text{O}_{\text{vac}}$ . Interestingly,  
371 the new peak centered at 530.4 eV in  $\text{O}1\text{s}$  spectra of LCO/Gr sample confirms the formation of surface  
372 Co–O–C bonds (Figure 3b, highlighted with an arrow). This peak results from the strong surface  
373 interaction between LCO and graphene [69]. Details are given in the supplementary material (Figure  
374 S5). In addition, EPR measurements were carried out to examine unpaired electrons in LCO, graphene,  
375 LCO+Gr, and LCO/Gr (Figure 3c). The broad EPR signal observed for LCO is assigned to the  
376 ferromagnetic (FM) clustering of the cobalt ions [70]. For the graphene sample, the narrow signal  
377 observed at  $g \approx 2.005$  can be tentatively assigned to the presence of conduction electrons and/or localized  
378 sigma “dangling bond” spins associated with defects. In case of LCO+Gr sample, the broad signal  
379 assigned to clustering of cobalt ions is decreased along with the presence of a small narrow signal  
380 appearing from the graphene sample. In contrast, the intensity of the narrow signal was increased for  
381 LCO/Gr sample. This confirmed reduced oxidation of cobalt ions in the LCO/Gr sample and thus further  
382 manifests the formation of  $\text{O}_{\text{vac}}$ .



383  
 384  
 385 Figure 3. a) XPS curve fit of Co<sub>2</sub>p and b) O<sub>1</sub>s of the LCO, LCO+Gr, and LCO/Gr powder and c) EPR spectra of  
 386 graphene, LCO, LCO+Gr, and LCO/Gr.

387 Furthermore, FTIR spectroscopy was carried out to confirm the formation of LCO/Gr nanocomposite  
 388 (See supplementary material Figure S6). In the FTIR spectrum of LCO, the peaks at  $\sim 550$  and  $590\text{ cm}^{-1}$   
 389 are assigned to characteristic Co–O stretching vibration and O–Co–O deformation modes of LaCoO<sub>3</sub>,  
 390 respectively [71], whereas the characteristic peaks at  $845$  and  $1540\text{ cm}^{-1}$ , and  $3200\text{--}3600\text{ cm}^{-1}$  are  
 391 attributed to symmetric and asymmetric COO<sup>-</sup> vibration and O–H stretching vibration [72,73].  
 392 However, after the introduction of graphene, the peak intensities of O–H and COO<sup>-</sup> groups decreased  
 393 significantly, suggesting that the O–H and COO<sup>-</sup> groups are substituted to form a Co–O–C bond  
 394 between LCO and graphene nanoparticles [74]. This robust interaction between LCO and graphene  
 395 nanoparticles is assumed to prevent cobalt leaching and mediates fast electron transport through the

396 graphene matrix to the LCO nanoparticles, enhancing their catalytic performance [42]. Besides, new  
397 absorption peaks in the 1380–1470  $\text{cm}^{-1}$  range and at 1640  $\text{cm}^{-1}$  are ascribed to aromatic carbon ring  
398 vibrations [75] and C=C stretching vibration [76], respectively, confirming the presence of graphene in  
399 LCO/Gr. Noteworthy, this result is consistent with TEM, XRD, Raman, and XPS analyses, altogether  
400 proving a strong interaction between LCO and graphene and thus the successful formation of a stable  
401 LCO/Gr composite.

### 402 **3.3 Electrochemical characterization of LCO/Gr nanocomposites**

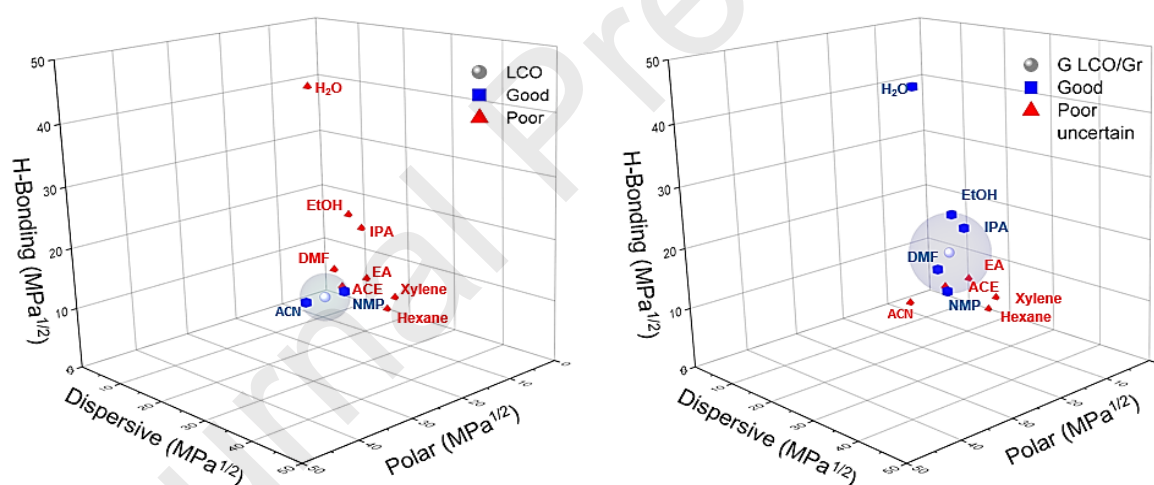
403 The interfacial and composite conductivity of the catalyst can affect its catalytic performance. Thus,  
404 electrochemical impedance spectroscopy was performed to evaluate the conductivity of the pure LCO  
405 catalysts (pressed pellets) and the LCO/Gr nanocomposite. The Argand diagram of LCO (Fig S7a)  
406 shows the typical characteristics of a polycrystalline oxide semiconductor and an equivalent circuit for  
407 the grain boundary and bulk conductivity consisting of two R/CPE elements could be fitted to the  
408 measured data. The observed conductivity is surprisingly high for a nanocrystalline semiconductor  
409 material, whose conductivity is dominated by grain boundary resistances.

410 The electrical behavior of the composite material (Fig S7b) is characterized by the very high  
411 conductivity of the graphene. All parasitic resistances of our 2-point experimental setup sum up to about  
412 1.2 Ohm, so that essentially Ohmic behavior is observed. Towards higher frequencies (from about  
413 1 kHz) inductive effects appear visibly, which can be fitted by a R/CPE. Compared to the known  
414 capacitive behavior, however, the phase angle of this CPE is shifted by about  $180^\circ$  to a capacitor, so that  
415 it acts as an inductor. Due to the combination of highly conductive graphene and electrically well-  
416 conducting LCO nanoparticles, a very good electrical contact of LCO nanoparticles and graphene can  
417 be assumed here, which we believe greatly promotes the catalytic performance of the LCO/Gr material.

### 418 **3.4 Stability of nanoparticle dispersions**

419 High dispersion stability of the generated catalysts is a key factor to achieve good catalytic activity  
420 during PMS activation. Hence, identifying appropriate parameters that distinguish surface

421 characteristics before and after graphene introduction is important. Hansen solubility parameters (HSP)  
 422 represent surface characteristics and were determined here using analytical centrifuge (AC) experiments  
 423 [55]. From the AC software (SEPView), we obtain optical transmission profiles (fingerprints) that can  
 424 be employed to calculate so-called stability trajectories (see supplementary material, Figure S8-9). These  
 425 enable to assess the interaction of the particle surface with the continuous phase and thus a categorization  
 426 of probe liquids into good and poor according to the nanoparticle dispersion stability (see supplementary  
 427 material, Table S3-S4). As shown in Figure 4, the dispersion stability of LCO/Gr was analyzed in five  
 428 probe liquids (water, dimethylformamide, isopropanol, acetonitrile, and N-methyl-2-pyrrolidone). In case  
 429 of LCO, the nanoparticles were well-dispersible in only two probe liquids (acetonitrile and N-methyl-  
 430 2-pyrrolidone). Finally derived HSP values are summarized in the Table 1. The strong difference between  
 431 LCO and LCO/Gr further corroborates the findings of the previous chapters regarding the successful  
 432 synthesis of stable LCO/Gr composites.



433  
 434 Figure 4. HSP sphere of LCO and LCO/Gr derived from HSPiP software and derived Hansen coordinates.

435 Table 1: HSP parameters of LCO and the range of HSP for LCO/Gr samples

Materials	LCO	LCO/Gr
Dispersive interactions $\delta_D$ (MPa <sup>1/2</sup> )	16.7	15.3 – 20.5
Dispersive interactions $\delta_P$ (MPa <sup>1/2</sup> )	15.2	8.4 – 15.4
Dispersive interactions $\delta_H$ (MPa <sup>1/2</sup> )	6.7	11.8 – 14.9
Sphere radius (MPa <sup>1/2</sup> )	4	6.8 – 15.3
Total combinations possible	-	1024
Combinations chosen for HSP	-	7 out of 8
Outliers	-	1

436

437 It needs to be mentioned that for deriving HSP, water was not considered due to its hydrogen bonding  
438 capabilities ( $\delta_H = 42$  MPa<sup>1/2</sup>) and hence its large distance compared to other solvents [77]. However,  
439 water is one of the most stable solvents for LCO/Gr, which is important for PMS activation. It is  
440 noteworthy to mention that the catalytic reaction was conducted in aqueous medium, suggesting that  
441 LCO/Gr might exhibit improved PMS activation compared to LCO which showed a poor dispersibility  
442 in water. This leads to agglomeration and sediments, and therefore additionally lowers the catalytic  
443 activity. Thus, dispersion studies in water were performed separately employing transmittograms (see  
444 supplementary materials, Figure S10). The LCO/Gr nanoparticles that are dispersed in tap water show  
445 the quickest sedimentation due to the presence of inorganic anions that interact with the nanoparticles  
446 surface and lead to poor dispersion. In contrast, the LCO/Gr nanoparticles dispersed in deionized water  
447 have the best dispersion stability, and even after 330 minutes, the full particles have not settled.  
448 However, when LCO/Gr particles were mixed with PMS, the dispersion stability of the LCO/Gr  
449 decreased significantly. This can be mainly attributed to a drop from pH 7 to 5 within a few minutes  
450 after the addition of PMS (see supplementary material, Figure S19).

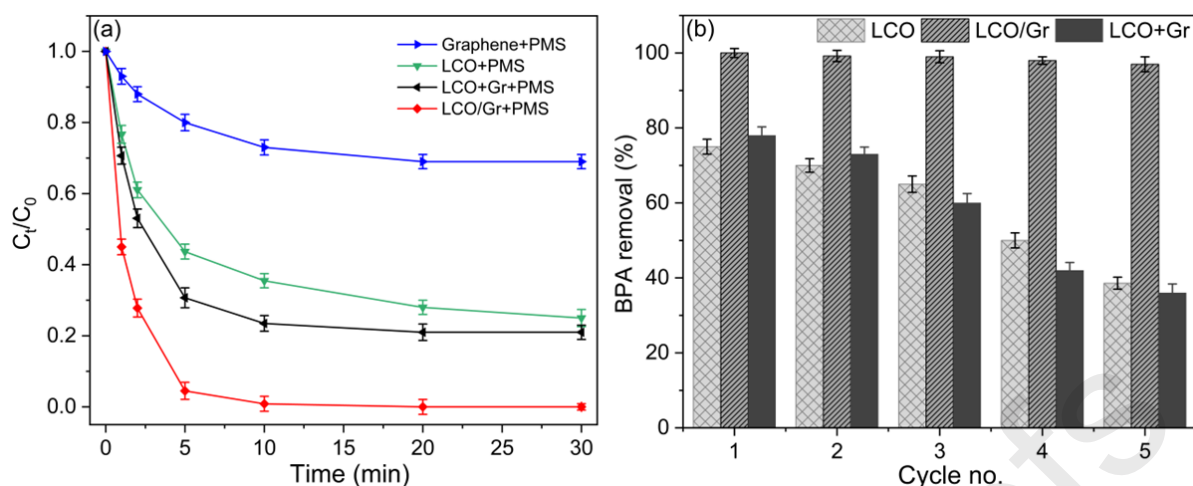
### 451 3.5 Catalytic performance and stability of catalysts

452 BPA, an endocrine-disrupting compound, is intensely used for the production of polycarbonate plastics  
453 and epoxy resins in the internal coatings of food packaging [78]. As a result of its widespread use, BPA  
454 is ubiquitously detected in food, drinking water, aquatic animals, and humans, and it decomposes only  
455 slowly under natural conditions [79]. Therefore, the catalytic performance of LCO/Gr was evaluated  
456 with regard to the degradation of BPA. 0.1 g/l LCO/Gr and a PMS concentration of 0.5 mmol/l was  
457 selected for subsequent experiments. Details are given in the supplementary material (Section 2, Figure  
458 S11-12).

459 The catalytic performance of LCO, graphene, and LCO/Gr nanoparticles was studied at pH 7 to  
460 understand the synergetic effect between LCO and graphene nanoparticles (Figure 5a). In the case of  
461 either LCO (0.1 g/l) or graphene (0.1 g/l) with PMS, the removal efficiency of BPA achieved 75 % and  
462 30 % within 30 min, respectively. Interestingly, the BPA degradation efficiency of the LCO+Gr+PMS  
463 (0.068 g/l LCO + 0.032 g/l graphene) system reached only 80 % within 30 min. In contrast, the  
464 LCO/Gr+PMS (0.1 g/l) system showed complete BPA degradation after about 10 min, indicating that  
465 the enhanced catalytic performance of LCO/Gr is based on a robust interaction between LCO and  
466 graphene and the presence of oxygen vacancies, as proven by Raman, XPS, and EPR studies. Based on  
467 Equation 2,  $k_{app}$  values of the BPA degradation were calculated as 0.17 and 0.52  $\text{min}^{-1}$  for LCO and  
468 LCO/Gr samples, respectively, confirming that the catalytic performance of the LCO/Gr catalyst is  
469 significantly higher than that of pure LCO material. We attribute the catalytic enhancement of LCO/Gr  
470 to the following features:

- 471 (i) The higher specific surface area of the LCO/Gr composite provides a better accessibility of active  
472 sites than pure LCO since the composite supports BPA molecules adsorption through strong  $\pi$ - $\pi$   
473 and hydrogen-bond interaction, leading to faster degradation of BPA.
- 474 (ii) The presence of unpaired  $\pi$  electrons in the LCO/Gr structure facilitates fast electron transport from  
475 LCO to PMS molecules through graphene nanosheets, supported by robust Co-O-C interactions  
476 that prevent cobalt leaching from LCO/Gr nanoparticles and therefore improve the catalytic  
477 performance of LCO/Gr.





478

479 Figure 5. a) BPA degradation with various catalysts in different reaction systems and b) stability tests of  
 480 LCO/Gr+PMS system. Reaction conditions: BPA = 40 mg/l; PMS = 0.5 mmol/l; Catalyst = 0.1 g/l; pH = 7.

481 The residual PMS concentration was varied during PMS activation in different systems (see  
 482 supplementary material, Figure S13). The concentration of residual PMS in the LCO+PMS and  
 483 LCO+Gr+PMS system was about 0.27 and 0.23 mmol/l, which attributed to about 54 and 46 % of the  
 484 initial PMS concentration, respectively. However, in the LCO/Gr+PMS system, the residual PMS  
 485 concentration declined to about 0.08 mmol/l (16 %). This result suggests that the LCO/Gr+PMS system  
 486 consumes more PMS which we attribute to the fast electron transport from PMS molecules to the LCO  
 487 through graphene nanosheets. Therefore, faster BPA degradation is achieved.

488 The reusability of catalysts is important to determine the catalyst stability for practical applications in  
 489 water treatment. To confirm the durability of the catalyst in the LCO/Gr+PMS system, five cycling  
 490 experiments were conducted under identical conditions. As displayed in Figure 5b, the reused LCO/Gr  
 491 catalyst presented higher catalytic activity and stability compared to LCO and LCO+Gr in all five  
 492 reaction runs. The insignificant decrease in BPA removal with LCO/Gr+PMS is due to the mass loss of  
 493 catalyst after washing during the recycling process. In addition, the mineralization extent of BPA  
 494 removal was measured for all catalytic tests by TOC measurements after 30 min. The TOC removal of  
 495 BPA was around 35 and 62 % for LCO and LCO/Gr catalysts, respectively, while the TOC removal of  
 496 BPA for LCO/Gr+PMS remains unabatedly high after five recycling operations (see supplementary



497 material, Figure S14). This indicates that the stable LCO/Gr+PMS system exhibits excellent catalytic  
498 performance through the multi-cycle process.

499 As an important catalyst characteristic, leaching of cobalt ions was investigated by AAS analysis during  
500 PMS activation. Despite the fact that both LCO+Gr+PMS and LCO+PMS exhibited good catalytic  
501 activity, the cobalt leaching amount (2.9 mg/l for LCO+Gr and 3.5 mg/l for LCO) is much higher than  
502 that with the LCO/Gr+PMS system (0.004 mg/l), which is clearly below the threshold limit value  
503 (0.05 mg/l) set by the World Health Organization (WHO) [80]. To investigate whether the leached  
504 cobalt shows some catalytic activity, the BPA removal efficiency using the  $\text{Co}^{2+}$ +PMS system was  
505 studied under the same conditions (see supplementary material, Figure S15). The BPA removal of the  
506 homogeneous  $\text{Co}^{2+}$ +PMS system was less than 4 %, suggesting that the high catalytic performance  
507 mainly benefitted from the heterogeneous LCO/Gr+PMS system. The unchanged chemical structure of  
508 the LCO/Gr catalyst after five runs also supports its high stability (see supplementary material, Figure  
509 S16). There is no change in the XRD diffraction pattern of the multiply-used catalyst as compared to  
510 pristine LCO/Gr. These results indicate that the LCO/Gr system is a much more eco-friendly, efficient,  
511 and effective catalyst for practical water treatment applications compared to previously reported  
512 heterogeneous carbon-supported catalysts as only a vanishingly small proportion of cobalt is lost with  
513 this catalyst material (Table 2).

514

515 Table 2: Comparison of the BPA removal by LCO/Gr in this work with those of other related carbon-supported  
 516 catalysts in the literature.

Catalyst	Dosage (mg/l)	BPA conc. (mg/l)	PMS conc (mmol/l)	BPA removal (%)	Time (min)	Metal leaching (mg/l)	References
Fe <sub>3</sub> C@NCNTs/ Gr	100	20	0.65	98	30	(Fe) ≈ 0.36	[81]
Co <sub>3</sub> O <sub>4</sub> /MXene	100	20	1	99	20	(Co) ≈ 0.36	[82]
CoS/Gr	100	20	0.32	92	8	(Co) ≈ 0.52	[83]
Fe <sub>3</sub> Co <sub>7</sub> /Gr	100	20	0.65	98	30	(Co) ≈ 3.30	[84]
Co <sub>3</sub> O <sub>4</sub> /MOFs	100	20	1.6	95	10	(Co) ≈ 0.35	[85]
LaFeO <sub>3</sub> /GO	500	20	2	100	60	(Fe) ≈ 0.24 (La) ≈ 0.88	[86]
Co <sub>3</sub> O <sub>4</sub> /CC	100	10	0.32	99	10	(Co) ≈ 0.25	[87]
LCO/Gr	100	40	0.32	100	10	(Co) ≈ 0.004	This work

### 517 3.6 Reactive species identification

518 To understand the catalytic mechanism of the LCO/Gr+PMS system, EPR spectra of solutions and XPS  
 519 spectra of LCO/Gr before and after catalytic experiments were recorded and analyzed. The contribution  
 520 of different reactive radicals such as SO<sub>4</sub><sup>•-</sup>, •OH, O<sub>2</sub><sup>•-</sup>, and <sup>1</sup>O<sub>2</sub> for BPA degradation was investigated by  
 521 adding commonly used radical scavengers like ethanol (EtOH), tert-butanol (TBA), p-benzoquinone  
 522 (BQ), and β-carotene (Crt). Here, EtOH was employed to scavenge both SO<sub>4</sub><sup>•-</sup> and •OH, TBA was used  
 523 to quench •OH [88], whereas Crt and BQ were chosen as scavengers of <sup>1</sup>O<sub>2</sub> and O<sub>2</sub><sup>•-</sup>, respectively [89].

524 As depicted in Figure 6a, the removal rate of BPA was decreased from 100 to 87 % when using 0.1 mol/l  
 525 EtOH and more inhibition (79 %) was observed with the addition of high concentration of 0.5 mol/l  
 526 EtOH. In contrast, no significant change in BPA removal was observed with the addition of 0.1 and  
 527 0.5 mol/l TBA. This suggests a minor contribution of SO<sub>4</sub><sup>•-</sup> and •OH to BPA degradation. Moreover, the

528 removal efficiency declined to 40 % when adding 5 mmol/l BQ. The addition of a small dose of Cr<sup>3+</sup> (0.5  
529 mmol/l) led to a BPA removal efficiency of only 26 %, indicating that <sup>1</sup>O<sub>2</sub> and O<sub>2</sub><sup>•-</sup> are the primary  
530 reactive species in the LCO/Gr+PMS system.

531 The pseudo-first-order constants with the addition of TBA and EtOH were calculated to determine the  
532 contribution of different reactive species in the LCO/Gr+PMS system. The contributions of <sup>•</sup>OH and  
533 SO<sub>4</sub><sup>•-</sup> radicals were calculated using the following equations (4-5) [90]:

$$534 \quad \lambda_{(\cdot\text{OH})} = (k_0 - k_1)/k_0 \quad (\text{Equation 4})$$

$$535 \quad \lambda_{(\text{SO}_4^{\cdot-})} = (k_1 - k_2)/k_0 \quad (\text{Equation 5})$$

536 where  $k_0$  is the rate constant of BPA degradation in LCO/Gr+PMS system without scavenger,  $k_1$  and  $k_2$   
537 are the rates constant for degradation of BPA by <sup>•</sup>OH and SO<sub>4</sub><sup>•-</sup>.

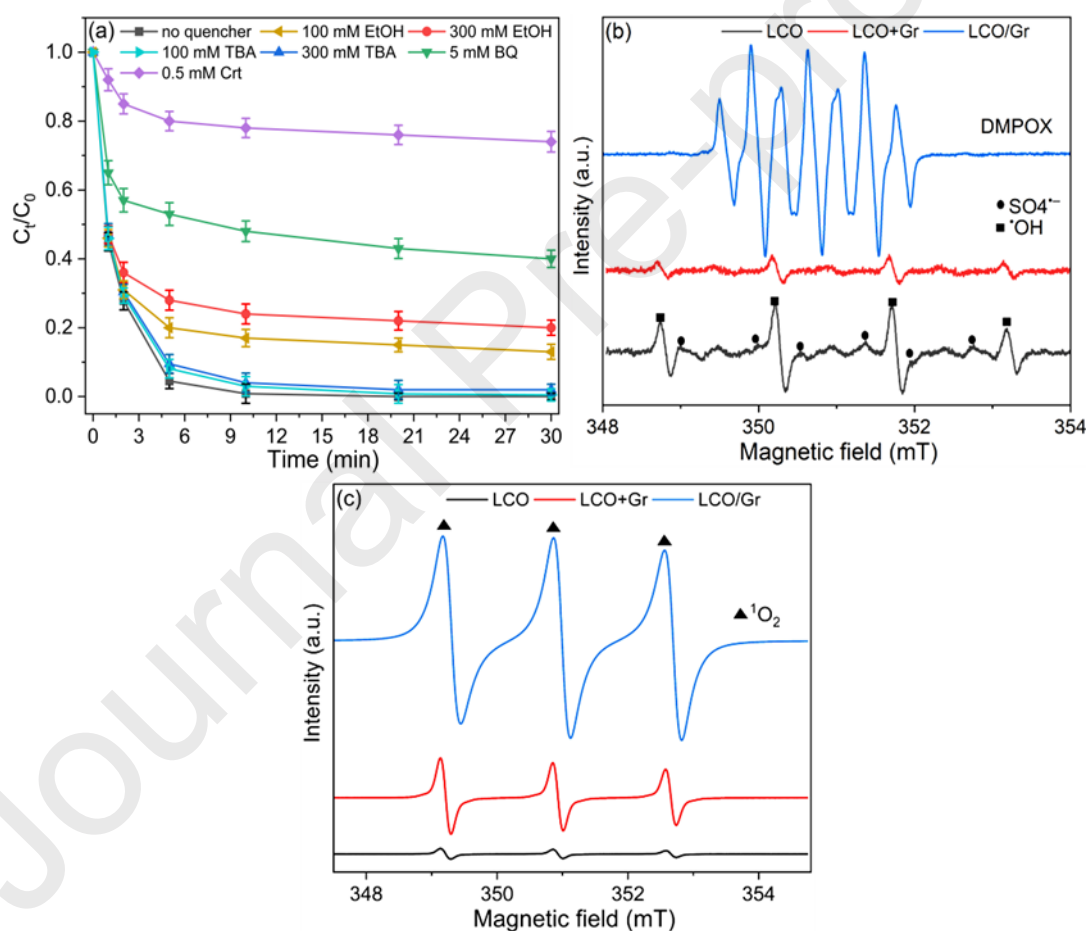
538 Since <sup>1</sup>O<sub>2</sub> might be generated from the oxidation of O<sub>2</sub><sup>•-</sup>, their common contributions ( $\lambda(\text{O}_2^{\cdot-}/^1\text{O}_2)$ )  
539 were estimated according to the following equation 6 [91]:

$$540 \quad \lambda_{\text{O}_2^{\cdot-}/^1\text{O}_2} = \lambda_{(\text{overall})} - (\lambda_{(\text{SO}_4^{\cdot-})} + \lambda_{(\cdot\text{OH})}) \quad (\text{Equation 6})$$

541 The values of  $k_0$ ,  $k_1$ , and  $k_2$  were calculated as 0.52, 0.45, and 0.28 min<sup>-1</sup>, respectively, according to  
542 equation 2. As a result, the relative contributions of <sup>•</sup>OH, SO<sub>4</sub><sup>•-</sup>, and <sup>1</sup>O<sub>2</sub>/O<sub>2</sub><sup>•-</sup> in the LCO/Gr+PMS  
543 systems were determined to 13.4, 32.6, and 54 %, respectively.

544 Furthermore, EPR tests using DMPO and TEMP as radical spin-trapping agents for SO<sub>4</sub><sup>•-</sup> and <sup>•</sup>OH, and  
545 <sup>1</sup>O<sub>2</sub>, respectively, were carried out to confirm the formation of reactive radicals from PMS activation.  
546 As shown in Figure 6b, when LCO+PMS were added, characteristic signals for DMPO-<sup>•</sup>OH adducts  
547 (with hyperfine splitting constants of  $\alpha_{\text{H}} = \alpha_{\text{N}} = 14.8$  G) and DMPO-SO<sub>4</sub><sup>•-</sup> adducts ( $\alpha_{\text{N}} = 13.2$  G,  $\alpha_{\text{N}} =$   
548 9.6 G,  $\alpha_{\text{H}} = 1.48$  G,  $\alpha_{\text{H}} = 0.78$  G) were observed, demonstrating the generation of both <sup>•</sup>OH and SO<sub>4</sub><sup>•-</sup>  
549 radicals by the LCO+PMS system. Similar results are obtained in the LCO+Gr+PMS system with  
550 reduced <sup>•</sup>OH and SO<sub>4</sub><sup>•-</sup> signals, due to a decrease in the LCO dosage (0.07 g/l LCO + 0.03 g/l graphene)  
551 compared to the LCO system (0.1 g/l). This suggests that there is no interaction between graphene and  
552 LCO nanoparticles. However, in case of LCO/Gr+PMS, the appearance of seven-line EPR adducts

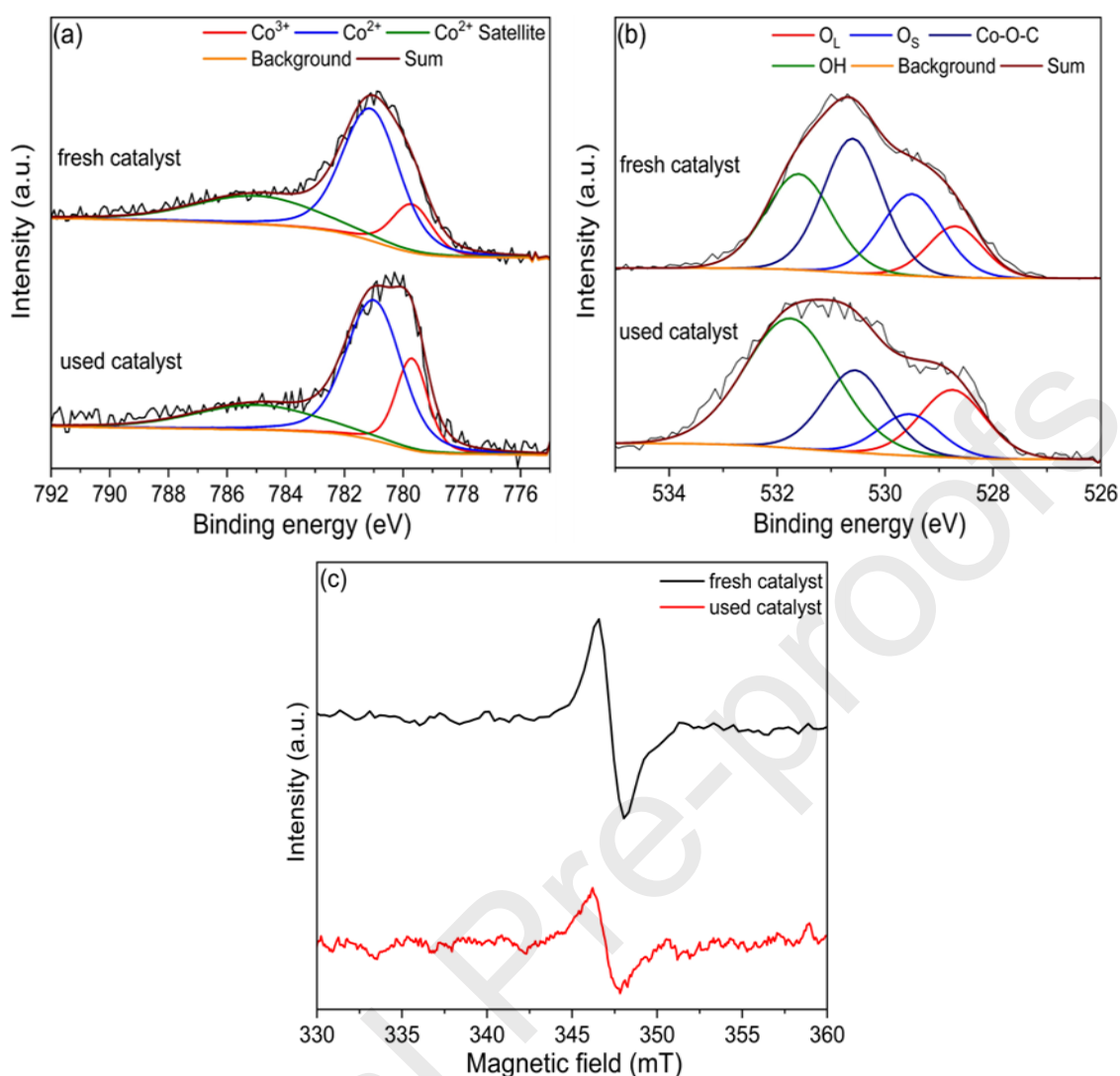
553 assigned to 5,5-dimethyl-1-pyrrolidone-2-oxyl (DMPOX) could be indexed to the direct oxidation of  
 554 DMPO with nonradical species  $^1\text{O}_2$  [92] (Figure 6b). Additionally, the characteristic triplet signal of the  
 555 TEMP- $^1\text{O}_2$  adduct ( $\alpha_N = 1.72$  mT) was observed when TEMP was added, confirming the presence of  
 556  $^1\text{O}_2$  in the LCO/Gr+PMS system (Figure 6c). The peak intensity of  $^1\text{O}_2$  in LCO/Gr+PMS system was  
 557 significantly higher than that of the LCO+PMS and LCO+Gr+PMS system, suggesting the boosted  
 558 generation of  $^1\text{O}_2$  which might be attributed to oxygen vacancies. These results are also consistent with  
 559 the radical scavenging experiments. Hence, it can be concluded that the nonradical pathway ( $^1\text{O}_2$ ) plays  
 560 a dominant role in the BPA degradation while the radical pathway ( $\text{SO}_4^{\cdot-}$  and  $\cdot\text{OH}$ ) contributes  
 561 significantly less.



562  
 563 Figure 6. a) Effect of different radical scavengers on the BPA degradation process with LCO/Gr+PMS. EPR  
 564 spectra using b) DMPO, and c) TEMP as the trapping agent for solutions with PMS, LCO/Gr and LCO/Gr+PMS,  
 565 respectively. Reaction conditions: BPA = 40 mg/l, PMS = 0.5 mmol/l, Catalyst = 0.1 g/l, DMPO = 50 mmol/l,  
 566 TEMP = 20 mmol/l.

### 567 3.7 Surface active site identification and possible mechanisms

568 To investigate the catalytic active sites of LCO/Gr, the activity of LCO/Gr was compared to that of gas-  
569 phase synthesized  $\text{Co}_3\text{O}_4$ ,  $\text{La}_2\text{O}_3$ ,  $\text{LaCoO}_3$ , and graphene (see supplementary material, Figure S17). The  
570 removal efficiency of BPA achieved less than 30 % with  $\text{La}_2\text{O}_3$ +PMS and graphene+PMS, which  
571 indicated that the La and C atoms of LCO/Gr were not the main active sites for BPA removal. In case  
572 of  $\text{Co}_3\text{O}_4$  and  $\text{LaCoO}_3$ , the BPA degradation efficiency reached 45 and 75 %, respectively, suggesting  
573 that the Co atom in the LCO/Gr catalyst structure can serve as the active center for BPA degradation.  
574 To identify the impact of Co in the PMS activation, XPS spectra of LCO/Gr before and after the catalytic  
575 reactions were studied. From fitting the spectra shown in Figure 7 it can be seen that the proportions of  
576  $\text{Co}^{2+}$  and  $\text{Co}^{3+}$  for the fresh catalyst were determined to be 85 and 15 %, while after the catalytic reaction  
577 the  $\text{Co}^{3+}$  content increased to 22 %. This indicates that the conversion process in the catalyst occurs at  
578 the LCO/Gr surface and  $\text{Co}^{2+}$  may participate in the activation of PMS. It is noteworthy that the addition  
579 of citric acid with cobalt-based catalysts during PMS activation can inhibit the degradation process due  
580 to formation of cobalt carboxyl complexes [93]. The addition of 2 mmol/l citric acid decreased the  
581 removal efficiency of BPA from 100 to 80 %, and the strong inhibition effect was observed with the  
582 increase of citric acid concentration (see supplementary material, Figure S18), further indicating that Co  
583 sites need to be considered as the active sites for PMS activation. Additionally, It has been reported that  
584  $\text{O}_{\text{vac}}$  can promote the bonding and electron transfer of PMS on the catalyst surface [94]. To ascertain the  
585 role of  $\text{O}_{\text{vac}}$  on the non-radical mechanism during PMS activation, the change of oxygen content before  
586 and after the reaction was analyzed (Figure 7b). From the O1s spectra, it could be deduced that the  
587 percentage of surface oxygen ( $\text{O}_s$ ) decreased from 23 to 14 % after the catalytic reaction, suggesting  
588 that  $\text{O}_{\text{vac}}$  played a dominant role in BPA degradation and was involved in generation of  $^1\text{O}_2$ . This finding  
589 is supported by analyzing the EPR spectra of fresh and used LCO/Gr catalyst after five reaction runs  
590 (Figure 7c). Compared with fresh LCO/Gr, the EPR signal of the used LCO/Gr was reduced, revealing  
591 that  $\text{O}_{\text{vac}}$  participated in PMS activation.

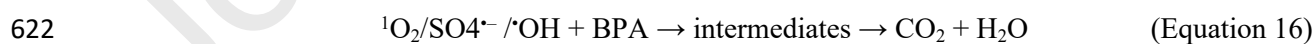
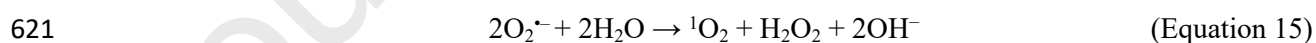
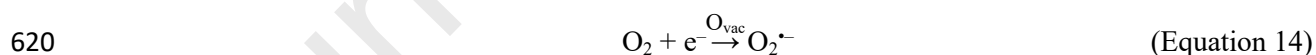
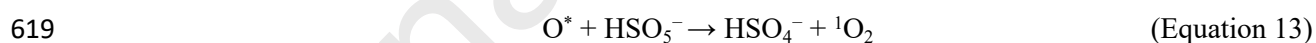
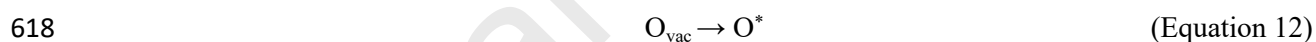
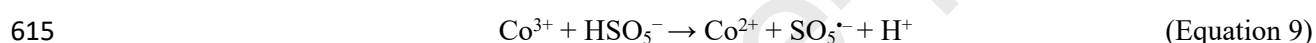
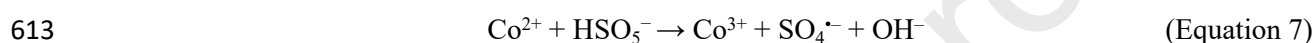


592

593 Figure 7. XPS spectra of (a) Co2p and (b) O1s for fresh and used LCO/Gr nanopowder, and c) EPR spectra of  
594 fresh and used LCO/Gr.

595 Based on the above results, a catalytic mechanism for BPA degradation by the LCO/Gr+PMS system is  
596 suggested including two reaction pathways: A radical ( $\text{SO}_4^{\cdot-}$  and  $\cdot\text{OH}$ ) and a non-radical process ( $^1\text{O}_2$ ).  
597 For the radical pathway,  $\text{SO}_4^{\cdot-}$  is generated through a reaction of PMS with the surface  $\text{Co}^{2+}$  of the  
598 LCO/Gr material (Equation 7) and consequently  $\cdot\text{OH}$  is produced from the reaction of  $\text{SO}_4^{\cdot-}$  with the  
599 hydroxide ion (Equation 8) [56]. The produced  $\text{Co}^{3+}$  will react with PMS molecules and convert to  $\text{Co}^{2+}$ ,  
600 since the standard potential value of the  $\text{Co}^{2+}/\text{Co}^{3+}$  redox pair (1.8 V) is higher than that of  $\text{HSO}_5^-/\text{SO}_5^{\cdot-}$   
601 (1.1 V) (Equation 9). Thus, the high catalytic performance through the multiple-cycle process can be  
602 achieved by the redox reaction of  $\text{Co}^{3+}/\text{Co}^{2+}$ . Moreover, as has been shown in Figure 7b, a hydroxylation  
603 of LCO/Gr occurs, which is attributed to the binding of water molecules to the catalyst surface during

604 PMS activation. Subsequently, these hydroxyl groups will combine with PMS to generate  $\text{SO}_4^{\cdot-}$   
 605 (Equation 10-11). The non-radical pathway (creation of  $^1\text{O}_2$ ) is mainly attributed to adsorbed oxygen of  
 606 metal oxide catalysts [95] and the direct oxidation or recombination of  $\text{O}_2^{\cdot-}$ . Therefore, the generation  
 607 of  $^1\text{O}_2$  can be attributed to the reaction of adsorbed oxygen species onto the surface vacancy, in which  
 608  $\text{O}_{\text{vac}}$  is converted to active oxygen ( $\text{O}^*$ ) leading to the formation of  $^1\text{O}_2$  (Equation 12-13) [96]. Moreover,  
 609 the quenching test results confirmed that  $\text{O}_2^{\cdot-}$  played a role in BPA degradation as explained before.  
 610 Thus, another possibility to generate  $^1\text{O}_2$  is the direct oxidation of  $\text{O}_2^{\cdot-}$  that is produced from the reaction  
 611 of  $\text{O}_2$  via  $\text{O}_{\text{vac}}$  (Equation 14-15). Finally, BPA can be attacked by the generated reactive oxygen species,  
 612 degrading into small molecular intermediates, and then converting into  $\text{CO}_2$  and  $\text{H}_2\text{O}$  (Equation 16).



## 623 3.8 Effect of reaction conditions on BPA degradation

### 624 3.8.1 Effect of initial pH

625 Since changing the pH will affect the surface functional groups of LCO/Gr material and PMS activation,  
626 changing the working pH range is expected to play a crucial role in the catalytic stability of the LCO/Gr  
627 material. Thus, the effect of pH on BPA degradation was analyzed ranging from pH = 3.0 to 11.0.  
628 Figure 8a depicts the influence of the initial pH on BPA removal. It is obvious that the BPA removal  
629 efficiency enhanced apparently within 10 min over a pH of 3 to 9 and is decreasing dramatically when  
630 the initial pH was adjusted to 11. Accordingly, the pseudo-first order rate constant ( $k_{app}$ ) of BPA  
631 degradation rises from 0.153 to 0.594  $\text{min}^{-1}$  when going from pH = 3 to 9 (see inset Figure 8a). However,  
632 when the initial pH of the solution was adjusted to 11, the  $k_{app}$  dropped to 0.075  $\text{min}^{-1}$ , which is about  
633 eight times lower than that of pH 9. To understand this phenomenon, the pH change with reaction time  
634 under different initial pH values during the PMS activation process was studied (see supplementary  
635 material, Figure S19). For initial pH values between 3 and 9, the pH drops sharply within a few minutes  
636 after the addition of PMS and decreases only slightly thereafter. For instance, when adjusting the pH to  
637 9, it dropped to 7.5 within 5 min and reached 6.8 after 30 min. In contrast, the pH of the solution with  
638 an initial pH of 11 maintained almost stable. This pH is higher than the  $\text{pH}_{\text{pzc}}$  of LCO/Gr nanoparticles  
639 (see supplementary material, Figure S20). Since the  $\text{pK}_{a1}$  of PMS is 0 and  $\text{pK}_{a2}$  is 9.4, PMS is present as  
640  $\text{HSO}_5^-$  under the investigated pH range of 0–9.4. Accordingly, for a pH of 11,  $\text{HSO}_5^-$  dissociates into  
641  $\text{SO}_5^{2-}$ , which diminishes the LCO/Gr catalytic efficiency due to the weak oxidative potential of  $\text{SO}_5^{2-}$   
642 [63]. Moreover, a high pH can result in the formation of C–OH,  $\text{La}(\text{OH})_3$ , and  $\text{Co}(\text{OH})_2$  (see  
643 supplementary material, Figure S21), causing the generation of  $\cdot\text{OH}$  from the reaction of  $\text{SO}_4^{\cdot-}$  with the  
644 hydroxide ion (Equation 5), which also can decrease the catalytic activity of LCO/Gr [97].

### 645 3.8.2 Effect of temperature

646 The effect of reaction temperature on BPA removal with the LCO/Gr+PMS system was studied at an  
647 initial pH of 7. As expected and shown in Figure 8b, the BPA degradation efficiency was enhanced with  
648 the increasing reaction temperature. As the reaction temperature increased from 25 to 55 °C, the  $k_{app}$



649 (1.05 min<sup>-1</sup>) is almost two times higher than at 25 °C (0.52 min<sup>-1</sup>). We attribute this result to the fast  
650 generation of reactive species by thermolytic rupture of O–O bond of PMS. The respective activation  
651 energy ( $E_a$ ) was determined from the Arrhenius equation:

$$652 \quad \ln k_{\text{app}} = \ln A - \frac{E_a}{RT} \quad (\text{Equation 17})$$

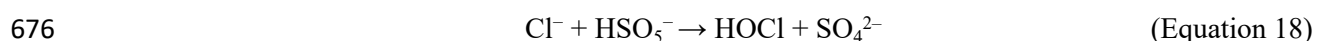
653 Where  $A$  is the pre-exponential factor,  $R$  is the universal gas constant (8.314 J mol<sup>-1</sup> K<sup>-1</sup>), and  $T$  is the  
654 solution temperature. The activation energy  $E_a$  of the LCO/Gr+PMS system was derived as 14 kJ/mol  
655 based on plotting  $\ln k_{\text{app}}$  against  $1/T$  (see inset, Figure 8b), which is much lower than the values reported  
656 for Co<sub>3</sub>O<sub>4</sub>/graphene (26.5 kJ/mol) [98] and MnFe<sub>2</sub>O<sub>4</sub>/graphene (25.7 kJ/mol) [99]. These findings imply  
657 that the reaction energy barrier for PMS activation is decreased in our LCO/Gr system indicating a  
658 higher catalytic activity and performance.

659

### 660 3.8.3 Effect of co-existing ions and NOM

661 Various inorganic anions are ubiquitous in real aquatic environments, which might affect the PMS  
662 activation in wastewater treatment as well [19]. Therefore, the effect of various anions relevant in  
663 aqueous systems (such as Cl<sup>-</sup>, NO<sub>3</sub><sup>-</sup>, H<sub>2</sub>PO<sub>4</sub><sup>-</sup>, HCO<sub>3</sub><sup>-</sup>, etc.) on the BPA removal with LCO/Gr  
664 nanoparticles was analyzed (Figure 8c and supplementary material Figure S22). The comparison of the  
665 respective results shows that the NO<sub>3</sub><sup>-</sup> anion had negligible adverse effects on BPA degradation, while  
666 the Cl<sup>-</sup> anions had a positive influence on BPA degradation. The positive effect of Cl<sup>-</sup> ions on BPA  
667 degradation may be attributed to the generation of active chlorine species (e.g. HOCl) which enhance  
668 BPA degradation [100] (Equation 18). Thus, to understand the impact of Cl<sup>-</sup> on BPA degradation, the  
669 BPA removal was analyzed in the presence of only PMS (see supplementary material, Figure S23a).  
670 The BPA removal efficiency was dramatically enhanced with 6 mg/ml Cl<sup>-</sup>, suggesting that HOCl was  
671 generated as a result of the reaction between PMS and Cl<sup>-</sup>. Besides, we evaluated the adsorption of BPA  
672 by LCO/Gr with the different Cl<sup>-</sup> concentrations (see supplementary material, Figure S23b). As before,  
673 20–23 % of BPA was adsorbed by LCO/Gr at different Cl<sup>-</sup> concentrations, indicating that the influence

674 of  $\text{Cl}^-$  on BPA adsorption was insignificant. Thus, we propose that the accelerated BPA degradation is  
675 based on the generation of HOCl along with  $^1\text{O}_2$  in the LCO/Gr+PMS+ $\text{Cl}^-$  system.



677 In contrast to  $\text{Cl}^-$  and  $\text{NO}_3^-$ ,  $\text{H}_2\text{PO}_4^-$  exhibits an inhibitory effect on BPA degradation efficiency because  
678 it can chelate with Co and form the Co-phosphate complex (see supplementary material, Figure S24),  
679 which in turn inhibits the PMS activation. Similarly, the removal efficiency of BPA was decreased with  
680 the addition of  $\text{HCO}_3^-$  due to the scavenging effect of  $\text{O}_2^{\cdot-}$ ,  $\text{SO}_4^{\cdot-}$ , and  $\cdot\text{OH}$  by  $\text{HCO}_3^-$  in the system,  
681 resulting in a decreased performance of the catalyst [101].

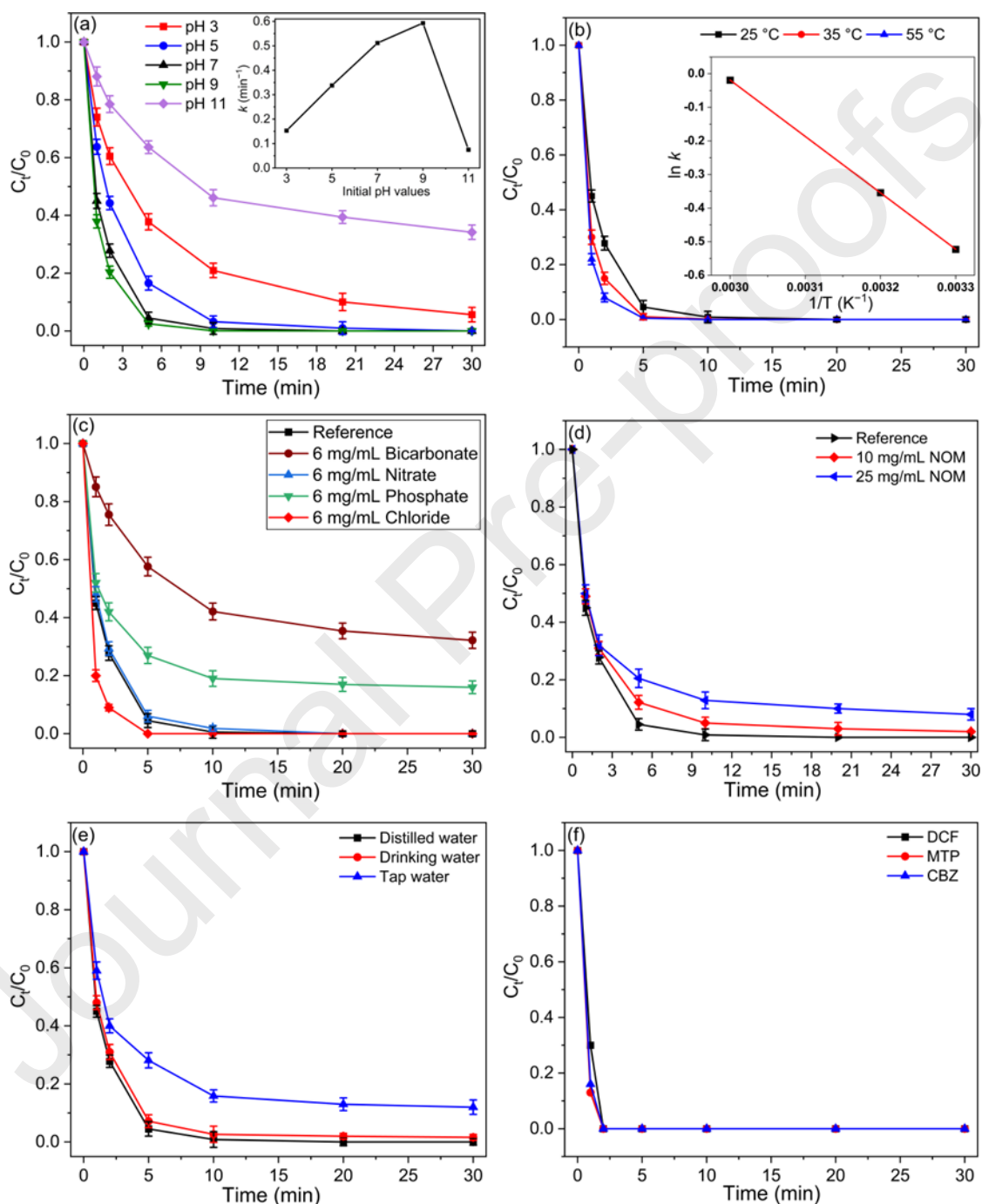
682 NOM is a constituent of all natural waters and soils and can consume a large number of reactive oxygen  
683 species such as  $\text{SO}_4^{\cdot-}$  and  $\cdot\text{OH}$  and block the active site on the catalyst surface during PMS activation  
684 [89], resulting in the decreased removal efficiency towards organic contaminants. As depicted in Figure  
685 8d, the removal rate of BPA was slightly inhibited with the presence of 10 and 25 mg/l NOM. The  
686 decrease might be related to the adsorption of NOM on the surface of the catalyst which could reduce  
687 the complexation of PMS to generate reactive oxygen species and is consistent with previous reports  
688 showing NOM to have a negligible impact on the performance of nonradical-based systems [102,103].

689 To evaluate the applicability of the LCO/Gr + PMS system in real aquatic environments, additional BPA  
690 removal experiments were conducted in tap and drinking water. The characteristics of tap and drinking  
691 water samples are depicted in Table S5. As shown in Figure 8e, the BPA removal efficiency was  
692 insignificantly decreased in the drinking water sample while the BPA degradation efficiency was  
693 slightly changed to 90 % in the tap water sample. The results indicate that the inorganic anions in the  
694 water have only negligible adverse effects on BPA degradation.

#### 695 **3.8.4 Effect of different pharmaceutical drugs**

696 Moreover, the catalytic performance of the LCO/Gr+PMS system has been tested for different kinds of  
697 drugs which is important for wastewater treatment applications. Hence, the catalytic activity of LCO/Gr  
698 was evaluated with diclofenac (DCF), metoprolol (MTP), and carbamazepine (CBZ). As shown in  
699 Figure 8f, the degradation of DCF, MTP, and CBZ reaches 100 % after 2 min, implying the

700 exceptionally high catalytic performance of the LCO/Gr+PMS system. The TOC removal of DCF, MTP,  
 701 and CBZ after 30 min was surprisingly high (57, 55, and 61 %, respectively, see supplementary material  
 702 Figure S25), proving that the LCO/Gr material is a promising catalyst for use in real wastewater  
 703 treatment systems.



704  
 705 Figure 8. Effects of (a) initial pH values, (b) temperature, (c) inorganic anions, (d) NOM, and (e) water matrices  
 706 BPA degradation by  $\text{La}_2\text{CoO}_{4+s}/\text{PMS}$ , and (f) the catalytic activity of LCO/Gr+PMS system on the removal of  
 707 various drugs. Reaction conditions: Drug/BPA = 40 mg/l; PMS = 0.5 mmol/l; Catalyst = 0.1 g/l; pH = 7.

### 708 3.9 Possible degradation pathways

709 The degradation pathway of BPA via the LCO/Gr+/PMS system was investigated and identified by LC-  
710 MS (see supplementary material, Figure S26). According to the mass spectrometric results, seven  
711 intermediates were detected for the BPA degradation using the LCO\Gr+PMS system (see  
712 supplementary material, table S6). First, BPA is mainly attacked by  $^1\text{O}_2$  to produce phenol and p-  
713 isopropyl phenol due to a  $\beta$ -scission of isopropyl between two phenyl groups in BPA [104]. Afterwards,  
714 the reaction products are further oxidized to form hydroquinone and 1-(4-methyl phenyl) ethenone,  
715 followed by a subsequent oxidative ring-opening leading to the formation of small-molecule  
716 intermediates including penta-1,4-dien-3-one, succinic acid, 1,5-hexadiene-3-ol, and 2-  
717 hydroxypropanoic acid. Finally, the small-molecule intermediates are further oxidized and mineralized  
718 into  $\text{CO}_2$  and  $\text{H}_2\text{O}$ .

## 719 4 Conclusions

720 In summary, we have demonstrated a robust and scalable method to synthesize LCO/Gr nanocomposites  
721 that have been employed as novel catalysts to activate PMS for different pollutants degradation. The  
722 developed approach consisting of a spray-flame synthesis method followed by the self-assembling  
723 technique has practical advantages such as scalability, reproducibility, easy control of the LCO size, and  
724 the subsequent decoration of the graphene nanosheets, eco-friendliness, and cost-effectivity.

725 The enhanced catalytic activity of the LCO/Gr composite compared to LCO nanoparticles is based on  
726 several, especially nano-specific features: First, we observed a synergistic and robust interaction  
727 between LCO and graphene, supported by stable Co–O–C interactions, leading to an outstanding BPA  
728 degradation efficiency (>99 %) and excellent stability with less cobalt leaching (0.004 mg/l) in the  
729 presence of PMS. Secondly, the high surface area of graphene (300  $\text{m}^2/\text{g}$ ) and the presence of unpaired  
730  $\pi$  electrons in the LCO/Gr structure facilitates a better accessibility of active sites, which is supported  
731 by a fast electron transport from LCO to PMS molecules through graphene nanosheets. Thirdly, LCO/Gr  
732 has an excellent catalytic activity through the multiple-cycle process (>95 %) and can be utilized over a  
733 wide pH range (pH 3-11). Fourthly, the LCO/Gr catalytic system exhibits a very effective removal of

734 different drugs such as diclofenac (>99 %), metoprolol (>99 %), and carbamazepine (>99 %), which are  
735 widely detected in municipal and industrial wastewater. Finally, the catalytic efficiency of LCO/Gr is  
736 insignificantly reduced in drinking water and tap water samples and showed high resistance to co-  
737 existing ions and NOM, proving that the LCO/Gr material is a promising catalyst for subsequent use in  
738 real wastewater treatment systems.

## 739 **Acknowledgement**

740 The results are based on work supported by the Mercator Research Center Ruhr (MERCUR) within the  
741 DIMENSION project. The authors thank M. Heidelmann from the Interdisciplinary Center for Analytics  
742 on the Nanoscale, ICAN, S. Apazeller (IVG UDE), R. Meckenstock (Faculty of Physics, UDE) for the  
743 TEM, TGA, and EPR measurements. A.K. Al-Kamal acknowledges the support of the German  
744 Academic Exchange Service (DAAD) as well as the IMPRS RECHARGE program of the Max-Planck  
745 Society. A.S. Amin gratefully acknowledges financial support from the Federal Ministry for Economic  
746 Affairs and Energy (WIPANO funding scheme, project number 03TN0013A). D. Segets thanks the  
747 Deutsche Forschungsgemeinschaft (DFG), grant number SE 2526/3-1 and H. Wiggers and C. Schulz  
748 thank the DFG through funding within projects 405366241 and 262219004. The authors are grateful to  
749 Alexander von Humboldt (AvH) Stiftung, Germany which financially supported this work.

## 750 **5 References**

- 751 [1] A. Küster, N. Adler, Pharmaceuticals in the environment: scientific evidence of risks and its  
752 regulation, *Philos. Trans. R. Soc. Lond. B. Biol. Sci.* 369 (2014) 20130587.  
753 <https://doi.org/10.1098/rstb.2013.0587>.
- 754 [2] W. Guo, B. Pan, S. Sakkiah, G. Yavas, W. Ge, W. Zou, W. Tong, H. Hong, Persistent Organic  
755 Pollutants in Food: Contamination Sources, Health Effects and Detection Methods, *Int. J.*  
756 *Environ. Res. Public Health.* 16 (2019) 4361. <https://doi.org/10.3390/ijerph16224361>.
- 757 [3] J. Wang, S. Wang, Reactive species in advanced oxidation processes: Formation, identification  
758 and reaction mechanism, *Chem. Eng. J.* 401 (2020) 126158.

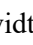
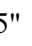
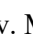
- 759 <https://doi.org/https://doi.org/10.1016/j.cej.2020.126158>.
- 760 [4] A. Fischbacher, C. von Sonntag, T.C. Schmidt, Hydroxyl radical yields in the Fenton process  
761 under various pH, ligand concentrations and hydrogen peroxide/Fe(II) ratios, *Chemosphere*.  
762 182 (2017) 738–744. <https://doi.org/https://doi.org/10.1016/j.chemosphere.2017.05.039>.
- 763 [5] M. Zhang, H. Dong, L. Zhao, D. Wang, D. Meng, A review on Fenton process for organic  
764 wastewater treatment based on optimization perspective, *Sci. Total Environ.* 670 (2019) 110–  
765 121. <https://doi.org/https://doi.org/10.1016/j.scitotenv.2019.03.180>.
- 766 [6] Q. Yang, Y. Ma, F. Chen, F. Yao, J. Sun, S. Wang, K. Yi, L. Hou, X. Li, D. Wang, Recent  
767 advances in photo-activated sulfate radical-advanced oxidation process (SR-AOP) for  
768 refractory organic pollutants removal in water, *Chem. Eng. J.* 378 (2019) 122149.  
769 <https://doi.org/https://doi.org/10.1016/j.cej.2019.122149>.
- 770 [7] Y. Liu, Y. Wang, Q. Wang, J. Pan, J. Zhang, Simultaneous removal of NO and SO<sub>2</sub> using  
771 vacuum ultraviolet light (VUV)/heat/peroxymonosulfate (PMS), *Chemosphere*. 190 (2018)  
772 431–441. <https://doi.org/https://doi.org/10.1016/j.chemosphere.2017.10.020>.
- 773 [8] R. Xie, J. Ji, K. Guo, D. Lei, Q. Fan, D.Y.C. Leung, H. Huang, Wet scrubber coupled with  
774 UV/PMS process for efficient removal of gaseous VOCs: Roles of sulfate and hydroxyl  
775 radicals, *Chem. Eng. J.* 356 (2019) 632–640.  
776 <https://doi.org/https://doi.org/10.1016/j.cej.2018.09.025>.
- 777 [9] Z.-H. Diao, Z.-Y. Lin, X.-Z. Chen, L. Yan, F.-X. Dong, W. Qian, L.-J. Kong, J.-J. Du, W. Chu,  
778 Ultrasound-assisted heterogeneous activation of peroxymonosulphate by natural pyrite for 2,4-  
779 dichlorophenol degradation in water: Synergistic effects, pathway and mechanism, *Chem. Eng.*  
780 *J.* (2019) 123771. <https://doi.org/https://doi.org/10.1016/j.cej.2019.123771>.
- 781 [10] H. Song, L. Yan, Y. Wang, J. Jiang, J. Ma, C. Li, G. Wang, J. Gu, P. Liu, Electrochemically  
782 activated PMS and PDS: Radical oxidation versus nonradical oxidation, *Chem. Eng. J.* (2019)  
783 123560. <https://doi.org/https://doi.org/10.1016/j.cej.2019.123560>.
- 784 [11] B. Bouzayani, E. Rosales, M. Pazos, S.C. Elaoud, M.A. Sanromán, Homogeneous and

- 785 heterogeneous peroxymonosulfate activation by transition metals for the degradation of  
786 industrial leather dye, *J. Clean. Prod.* 228 (2019) 222–230.  
787 <https://doi.org/https://doi.org/10.1016/j.jclepro.2019.04.217>.
- 788 [12] Z. Li, M. Wang, C. Jin, J. Kang, J. Liu, H. Yang, Y. Zhang, Q. Pu, Y. Zhao, M. You, Z. Wu,  
789 Synthesis of novel Co<sub>3</sub>O<sub>4</sub> hierarchical porous nanosheets via corn stem and MOF-Co  
790 templates for efficient oxytetracycline degradation by peroxymonosulfate activation, *Chem.*  
791 *Eng. J.* 392 (2020) 123789. <https://doi.org/https://doi.org/10.1016/j.cej.2019.123789>.
- 792 [13] S. Chen, J. Deng, C. Ye, C. Xu, L. Huai, J. Li, X. Li, Simultaneous removal of para-arsanilic  
793 acid and the released inorganic arsenic species by CuFe<sub>2</sub>O<sub>4</sub> activated peroxymonosulfate  
794 process, *Sci. Total Environ.* 742 (2020) 140587.  
795 <https://doi.org/https://doi.org/10.1016/j.scitotenv.2020.140587>.
- 796 [14] S. Ben Hammouda, F. Zhao, Z. Safaei, V. Srivastava, D. Lakshmi Ramasamy, S. Iftekhar, S.  
797 kalliola, M. Sillanpää, Degradation and mineralization of phenol in aqueous medium by  
798 heterogeneous monopersulfate activation on nanostructured cobalt based-perovskite catalysts  
799 ACoO<sub>3</sub> (A=La, Ba, Sr and Ce): Characterization, kinetics and mechanism study, *Appl. Catal.*  
800 *B Environ.* 215 (2017) 60–73. <https://doi.org/https://doi.org/10.1016/j.apcatb.2017.05.051>.
- 801 [15] J. Cao, L. Lai, B. Lai, G. Yao, X. Chen, L. Song, Degradation of tetracycline by  
802 peroxymonosulfate activated with zero-valent iron: Performance, intermediates, toxicity and  
803 mechanism, *Chem. Eng. J.* 364 (2019) 45–56.  
804 <https://doi.org/https://doi.org/10.1016/j.cej.2019.01.113>.
- 805 [16] S. Wang, J. Wang, Kinetics of PMS activation by graphene oxide and biochar, *Chemosphere.*  
806 239 (2020) 124812. <https://doi.org/https://doi.org/10.1016/j.chemosphere.2019.124812>.
- 807 [17] C. Cheng, S. Gao, J. Zhu, G. Wang, L. Wang, X. Xia, Enhanced performance of LaFeO<sub>3</sub>  
808 perovskite for peroxymonosulfate activation through strontium doping towards 2,4-D  
809 degradation, *Chem. Eng. J.* 384 (2020) 123377.  
810 <https://doi.org/https://doi.org/10.1016/j.cej.2019.123377>.



- 811 [18] Y. Wang, Z. Chi, C. Chen, C. Su, D. Liu, Y. Liu, X. Duan, S. Wang, Facet- and defect-  
812 dependent activity of perovskites in catalytic evolution of sulfate radicals, *Appl. Catal. B*  
813 *Environ.* 272 (2020) 118972. [https://doi.org/https://doi.org/10.1016/j.apcatb.2020.118972](https://doi.org/10.1016/j.apcatb.2020.118972).
- 814 [19] M. Hammad, B. Alkan, A. k. Al-kamal, M. Yusuf Ali, C. Kim, H. T. A. Wiedemann, D.  
815 Klippert, T.C. Schmidt, C. W. M. Kay, H. Wiggers, Enhanced heterogeneous activation of  
816 peroxymonosulfate by Ruddlesden-Popper-type  $\text{La}_2\text{CoO}_{4+\delta}$  nanoparticles for bisphenol A  
817 degradation, *Chem. Eng. J.* (2021) 131447.  
818 [https://doi.org/https://doi.org/10.1016/j.cej.2021.131447](https://doi.org/10.1016/j.cej.2021.131447).
- 819 [20] X. Duan, C. Su, J. Miao, Y. Zhong, Z. Shao, S. Wang, H. Sun, Insights into perovskite-  
820 catalyzed peroxymonosulfate activation: Maneuverable cobalt sites for promoted evolution of  
821 sulfate radicals, *Appl. Catal. B Environ.* 220 (2018) 626–634.  
822 [https://doi.org/https://doi.org/10.1016/j.apcatb.2017.08.088](https://doi.org/10.1016/j.apcatb.2017.08.088).
- 823 [21] B. Alkan, S. Cychy, S. Varhade, M. Muhler, C. Schulz, W. Schuhmann, H. Wiggers, C.  
824 Andronesco, Spray-Flame-Synthesized  $\text{LaCo}_{1-x}\text{Fe}_x\text{O}_3$  Perovskite Nanoparticles as  
825 Electrocatalysts for Water and Ethanol Oxidation, *ChemElectroChem.* 6 (2019) 4266–4274.  
826 <https://doi.org/10.1002/celec.201900168>.
- 827 [22] J. Bucker, B. Alkan, Q. Fu, W. Xia, J. Schulwitz, D. Waffel, T. Falk, C. Schulz, H. Wiggers, M.  
828 Muhler, B. Peng, Selective cyclohexene oxidation with  $\text{O}_2$ ,  $\text{H}_2\text{O}_2$  and tert-butyl hydroperoxide  
829 over spray-flame synthesized  $\text{LaCo}_{1-x}\text{Fe}_x\text{O}_3$  nanoparticles, *Catal. Sci. Technol.* 10 (2020)  
830 5196–5206. <https://doi.org/10.1039/D0CY00906G>.
- 831 [23] H. Chen, W. Cui, D. Li, Q. Tian, J. He, Q. Liu, X. Chen, M. Cui, X. Qiao, Z. Zhang, J. Tang,  
832 Z. Fei, Selectively Etching Lanthanum to Engineer Surface Cobalt-Enriched  $\text{LaCoO}_3$   
833 Perovskite Catalysts for Toluene Combustion, *Ind. Eng. Chem. Res.* 59 (2020) 10804–10812.  
834 <https://doi.org/10.1021/acs.iecr.0c01182>.
- 835 [24] Y. Yamada, K. Yano, D. Hong, S. Fukuzumi,  $\text{LaCoO}_3$  acting as an efficient and robust catalyst  
836 for photocatalytic water oxidation with persulfate, *Phys. Chem. Chem. Phys.* 14 (2012) 5753–



- 837 5760. <https://doi.org/10.1039/C2CP00022A>.
- 838 [25] P. Liang, D. Meng, Y. Liang, Z. Wang, C. Zhang, S. Wang, Z. Zhang, Cation deficiency tuned  
839  $\text{LaCoO}_{3-\delta}$  perovskite for peroxymonosulfate activation towards bisphenol A degradation,  
840 Chem. Eng. J. 409 (2021) 128196. <https://doi.org/https://doi.org/10.1016/j.cej.2020.128196>.
- 841 [26] X. Huang, G. Zhao, G. Wang, J.T.S. Irvine, Synthesis and applications of nanoporous  
842 perovskite metal oxides, Chem. Sci. 9 (2018) 3623–3637.  
843 <https://doi.org/10.1039/C7SC03920D>.
- 844 [27] S. Royer, D. Duprez, F. Can, X. Courtois, C. Batiot-Dupeyrat, S. Laassiri, H. Alamdari,  
845 Perovskites as Substitutes of Noble Metals for Heterogeneous Catalysis: Dream or Reality,  
846 Chem. Rev. 114 (2014) 10292–10368. <https://doi.org/10.1021/cr500032a>.
- 847 [28] P. Granger, V.I. Parvulescu, S. Kaliaguine, W. Prellier, Perovskites and Related Mixed Oxides,  
848 Wiley-VCH Verlag GmbH & Co. KGaA, 2016. [https://hal-normandie-univ.archives-](https://hal-normandie-univ.archives-ouvertes.fr/hal-02185521)  
849 [ouvertes.fr/hal-02185521](https://hal-normandie-univ.archives-ouvertes.fr/hal-02185521).
- 850 [29] N.T. Thuy, D. Le Minh, Size Effect on the Structural and Magnetic Properties of Nanosized  
851 Perovskite   $\text{LaCoO}_{3-\delta}$   
852   $\text{LaCoO}_{3-\delta}$   
853   $\text{LaCoO}_{3-\delta}$ , Adv. Mater. Sci. Eng. 2012 (2012)  
854 380306. <https://doi.org/10.1155/2012/380306>.
- 855 [30] B. Alkan, D. Medina, J. Landers, M. Heidelmann, U. Hagemann, S. Salamon, C. Andronescu,  
856 H. Wende, C. Schulz, W. Schuhmann, H. Wiggers, Spray-Flame-Prepared  $\text{LaCo}_{1-x}\text{Fe}_x\text{O}_3$   
857 Perovskite Nanoparticles as Active OER Catalysts: Influence of Fe Content and Low-  
858 Temperature Heating, ChemElectroChem. 7 (2020) 2564–2574.  
859 <https://doi.org/https://doi.org/10.1002/celec.201902051>.
- 860 [31] S. Angel, J.D. Tapia, J. Gallego, U. Hagemann, H. Wiggers, Spray-Flame Synthesis of  
861  $\text{LaMnO}_{3+\delta}$  Nanoparticles for Selective CO Oxidation (SELOX), Energy & Fuels. 35 (2021)  
862 4367–4376. <https://doi.org/10.1021/acs.energyfuels.0c03659>.

- 863 [32] C. Schulz, T. Dreier, M. Fikri, H. Wiggers, Gas-phase synthesis of functional nanomaterials:  
864 Challenges to kinetics, diagnostics, and process development, *Proc. Combust. Inst.* 37 (2019)  
865 83–108. <https://doi.org/https://doi.org/10.1016/j.proci.2018.06.231>.
- 866 [33] M. Abdul Nasir Khan, P. Kwame Klu, C. Wang, W. Zhang, R. Luo, M. Zhang, J. Qi, X. Sun,  
867 L. Wang, J. Li, Metal-organic framework-derived hollow Co<sub>3</sub>O<sub>4</sub>/carbon as efficient catalyst  
868 for peroxymonosulfate activation, *Chem. Eng. J.* 363 (2019) 234–246.  
869 <https://doi.org/https://doi.org/10.1016/j.cej.2019.01.129>.
- 870 [34] C. Liu, L. Liu, X. Tian, Y. Wang, R. Li, Y. Zhang, Z. Song, B. Xu, W. Chu, F. Qi, A. Ikhlaq,  
871 Coupling metal–organic frameworks and g-C<sub>3</sub>N<sub>4</sub> to derive Fe@N-doped graphene-like carbon  
872 for peroxymonosulfate activation: Upgrading framework stability and performance, *Appl.*  
873 *Catal. B Environ.* 255 (2019) 117763.  
874 <https://doi.org/https://doi.org/10.1016/j.apcatb.2019.117763>.
- 875 [35] W. Han, D. Li, M. Zhang, H. Ximin, X. Duan, S. Liu, S. Wang, Photocatalytic activation of  
876 peroxymonosulfate by surface-tailored carbon quantum dots, *J. Hazard. Mater.* 395 (2020)  
877 122695. <https://doi.org/https://doi.org/10.1016/j.jhazmat.2020.122695>.
- 878 [36] W. Lin, X. Xie, X. Wang, Y. Wang, D. Segets, J. Sun, Efficient adsorption and sustainable  
879 degradation of gaseous acetaldehyde and o-xylene using rGO-TiO<sub>2</sub> photocatalyst, *Chem. Eng.*  
880 *J.* 349 (2018) 708–718. <https://doi.org/https://doi.org/10.1016/j.cej.2018.05.107>.
- 881 [37] N. Baig, Ihsanullah, M. Sajid, T.A. Saleh, Graphene-based adsorbents for the removal of toxic  
882 organic pollutants: A review, *J. Environ. Manage.* 244 (2019) 370–382.  
883 <https://doi.org/https://doi.org/10.1016/j.jenvman.2019.05.047>.
- 884 [38] J. Xu, L. Wang, Y. Zhu, Decontamination of Bisphenol A from Aqueous Solution by Graphene  
885 Adsorption, *Langmuir.* 28 (2012) 8418–8425. <https://doi.org/10.1021/la301476p>.
- 886 [39] Q. Xiang, J. Yu, M. Jaroniec, Graphene-based semiconductor photocatalysts, *Chem. Soc. Rev.*  
887 41 (2012) 782–796. <https://doi.org/10.1039/C1CS15172J>.
- 888 [40] N. Zhang, M.-Q. Yang, S. Liu, Y. Sun, Y.-J. Xu, Waltzing with the Versatile Platform of

- 889 Graphene to Synthesize Composite Photocatalysts, *Chem. Rev.* 115 (2015) 10307–10377.  
890 <https://doi.org/10.1021/acs.chemrev.5b00267>.
- 891 [41] A. V Karim, A. Selvaraj, Graphene composites in photocatalytic oxidation of aqueous organic  
892 contaminants – A state of art, *Process Saf. Environ. Prot.* 146 (2021) 136–160.  
893 <https://doi.org/https://doi.org/10.1016/j.psep.2020.08.042>.
- 894 [42] M. Hammad, P. Fortugno, S. Hardt, C. Kim, S. Salamon, T.C. Schmidt, H. Wende, C. Schulz,  
895 H. Wiggers, Large-scale synthesis of iron oxide/graphene hybrid materials as highly efficient  
896 photo-Fenton catalyst for water remediation, *Environ. Technol. Innov.* (2020) 101239.  
897 <https://doi.org/https://doi.org/10.1016/j.eti.2020.101239>.
- 898 [43] U.K. Sur, Graphene: A Rising Star on the Horizon of Materials Science, *Int. J. Electrochem.*  
899 2012 (2012) 237689. <https://doi.org/10.1155/2012/237689>.
- 900 [44] C. Wang, P. Shi, X. Cai, Q. Xu, X. Zhou, X. Zhou, D. Yang, J. Fan, Y. Min, H. Ge, W. Yao,  
901 Synergistic Effect of Co<sub>3</sub>O<sub>4</sub> Nanoparticles and Graphene as Catalysts for Peroxymonosulfate-  
902 Based Orange II Degradation with High Oxidant Utilization Efficiency, *J. Phys. Chem. C.* 120  
903 (2016) 336–344. <https://doi.org/10.1021/acs.jpcc.5b10032>.
- 904 [45] V. Murugadoss, P. Panneerselvam, C. Yan, Z. Guo, S. Angaiah, A simple one-step  
905 hydrothermal synthesis of cobaltnickel selenide/graphene nanohybrid as an advanced platinum  
906 free counter electrode for dye sensitized solar cell, *Electrochim. Acta.* 312 (2019) 157–167.  
907 <https://doi.org/https://doi.org/10.1016/j.electacta.2019.04.142>.
- 908 [46] F. Yang, J. Mao, S. Li, J. Yin, J. Zhou, W. Liu, Cobalt–graphene nanomaterial as an efficient  
909 catalyst for selective hydrogenation of 5-hydroxymethylfurfural into 2,5-dimethylfuran, *Catal.*  
910 *Sci. Technol.* 9 (2019) 1329–1333. <https://doi.org/10.1039/C9CY00330D>.
- 911 [47] M. Khan, M.N. Tahir, S.F. Adil, H.U. Khan, M.R.H. Siddiqui, A.A. Al-warthan, W. Tremel,  
912 Graphene based metal and metal oxide nanocomposites: synthesis, properties and their  
913 applications, *J. Mater. Chem. A.* 3 (2015) 18753–18808. <https://doi.org/10.1039/C5TA02240A>.
- 914 [48] J. Liu, J. Tang, J.J. Gooding, Strategies for chemical modification of graphene and applications

- 915 of chemically modified graphene, *J. Mater. Chem.* 22 (2012) 12435–12452.  
916 <https://doi.org/10.1039/C2JM31218B>.
- 917 [49] Y. Chen, X. Bai, Y. Ji, T. Shen, Reduced graphene oxide-supported hollow Co<sub>3</sub>O<sub>4</sub>@N-doped  
918 porous carbon as peroxymonosulfate activator for sulfamethoxazole degradation, *Chem. Eng. J.*  
919 430 (2022) 132951. <https://doi.org/https://doi.org/10.1016/j.cej.2021.132951>.
- 920 [50] J. Ye, D. Yang, J. Dai, C. Li, Y. Yan, Confinement of ultrafine Co<sub>3</sub>O<sub>4</sub> nanoparticles in  
921 nitrogen-doped graphene-supported macroscopic microspheres for ultrafast catalytic oxidation:  
922 Role of oxygen vacancy and ultrasmall size effect, *Sep. Purif. Technol.* 281 (2022) 119963.  
923 <https://doi.org/https://doi.org/10.1016/j.seppur.2021.119963>.
- 924 [51] Y. Yao, Y. Hu, H. Hu, L. Chen, M. Yu, M. Gao, S. Wang, Metal-free catalysts of graphitic  
925 carbon nitride–covalent organic frameworks for efficient pollutant destruction in water, *J.*  
926 *Colloid Interface Sci.* 554 (2019) 376–387.  
927 <https://doi.org/https://doi.org/10.1016/j.jcis.2019.07.002>.
- 928 [52] S. Hardt, I. Wlokas, C. Schulz, H. Wiggers, Impact of ambient pressure on titania nanoparticle  
929 formation during spray-flame synthesis, *J. Nanosci. Nanotechnol.* 15 (2015) 9449–9456.  
930 <https://doi.org/10.1166/jnn.2015.10607>.
- 931 [53] F. Schneider, S. Suleiman, J. Menser, E. Borukhovich, I. Wlokas, A. Kempf, H. Wiggers, C.  
932 Schulz, SpraySyn—A standardized burner configuration for nanoparticle synthesis in spray  
933 flames, *Rev. Sci. Instrum.* 90 (2019) 85108. <https://doi.org/10.1063/1.5090232>.
- 934 [54] A. Münzer, L. Xiao, Y.H. Sehleier, C. Schulz, H. Wiggers, All gas-phase synthesis of  
935 graphene: Characterization and its utilization for silicon-based lithium-ion batteries,  
936 *Electrochim. Acta.* 272 (2018) 52–59.  
937 <https://doi.org/https://doi.org/10.1016/j.electacta.2018.03.137>.
- 938 [55] S. Bapat, D. Segets, Sedimentation Dynamics of Colloidal Formulations through Direct  
939 Visualization: Implications for Fuel Cell Catalyst Inks, *ACS Appl. Nano Mater.* 3 (2020)  
940 7384–7391. <https://doi.org/10.1021/acsanm.0c01467>.

- 941 [56] C. Liang, C.-F. Huang, N. Mohanty, R.M. Kurakalva, A rapid spectrophotometric  
942 determination of persulfate anion in ISCO, *Chemosphere*. 73 (2008) 1540–1543.  
943 <https://doi.org/https://doi.org/10.1016/j.chemosphere.2008.08.043>.
- 944 [57] L. Tepech-Carrillo, A. Escobedo-Morales, A. Pérez-Centeno, E. Chigo-Anota, J.F. Sánchez-  
945 Ramírez, E. López-Apreza, J. Gutiérrez-Gutiérrez, Preparation of Nanosized LaCoO<sub>3</sub> through  
946 Calcination of a Hydrothermally Synthesized Precursor, *J. Nanomater.* 2016 (2016) 6917950.  
947 <https://doi.org/10.1155/2016/6917950>.
- 948 [58] M.A. Pimenta, G. Dresselhaus, M.S. Dresselhaus, L.G. Cançado, A. Jorio, R. Saito, Studying  
949 disorder in graphite-based systems by Raman spectroscopy, *Phys. Chem. Chem. Phys.* 9 (2007)  
950 1276–1290. <https://doi.org/10.1039/B613962K>.
- 951 [59] T. Ishimoto, Y. Ito, T. Tada, R. Oike, T. Nakamura, K. Amezawa, M. Koyama, Theoretical  
952 study on temperature effect of electronic structure and spin state in LaCoO<sub>3</sub> by using density  
953 functional theory, *Solid State Ionics*. 285 (2016) 195–201.  
954 <https://doi.org/https://doi.org/10.1016/j.ssi.2015.08.017>.
- 955 [60] F. Cheng, T. Zhang, Y. Zhang, J. Du, X. Han, J. Chen, Enhancing Electrocatalytic Oxygen  
956 Reduction on MnO<sub>2</sub> with Vacancies, *Angew. Chemie Int. Ed.* 52 (2013) 2474–2477.  
957 <https://doi.org/https://doi.org/10.1002/anie.201208582>.
- 958 [61] J. Hu, X. Zeng, G. Wang, B. Qian, Y. Liu, X. Hu, B. He, L. Zhang, X. Zhang, Modulating  
959 mesoporous Co<sub>3</sub>O<sub>4</sub> hollow nanospheres with oxygen vacancies for highly efficient  
960 peroxymonosulfate activation, *Chem. Eng. J.* 400 (2020) 125869.  
961 <https://doi.org/https://doi.org/10.1016/j.cej.2020.125869>.
- 962 [62] C. Santhosh, A. Malathi, E. Daneshvar, P. Kollu, A. Bhatnagar, Photocatalytic degradation of  
963 toxic aquatic pollutants by novel magnetic 3D-TiO<sub>2</sub>@HPGA nanocomposite, *Sci. Rep.* 8  
964 (2018) 15531. <https://doi.org/10.1038/s41598-018-33818-9>.
- 965 [63] P.H.T. Ngamou, K. Kohse-Höinghaus, N. Bahlawane, CO and ethanol oxidation over LaCoO<sub>3</sub>  
966 planar model catalysts: Effect of the thickness, *Catal. Commun.* 12 (2011) 1344–1350.

- 967 <https://doi.org/https://doi.org/10.1016/j.catcom.2011.04.029>.
- 968 [64] C. Lv, H. Chen, M. Hu, T. Ai, H. Fu, Nano-oxides washcoat for enhanced catalytic oxidation  
969 activity toward the perovskite-based monolithic catalyst, *Environ. Sci. Pollut. Res.* 28 (2021)  
970 37142–37157. <https://doi.org/10.1007/s11356-021-13354-2>.
- 971 [65] L. Armelao, M. Bettinelli, G. Bottaro, D. Barreca, E. Tondello, LaCoO<sub>3</sub> Nanopowders by XPS,  
972 *Surf. Sci. Spectra.* 8 (2001) 24–31. <https://doi.org/10.1116/11.20010701>.
- 973 [66] M. Guiotto, M. Pacella, G. Perin, A. Iovino, N. Michelon, M.M. Natile, A. Glisenti, P. Canu,  
974 Washcoating vs. direct synthesis of LaCoO<sub>3</sub> on monoliths for environmental applications,  
975 *Appl. Catal. A Gen.* 499 (2015) 146–157.  
976 <https://doi.org/https://doi.org/10.1016/j.apcata.2015.04.013>.
- 977 [67] Y. Li, L. Liu, Z. Wang, L. Zhou, Y. Lan, C. Chen, Simultaneous oxidation of 4-  
978 aminophenylarsonic acid and adsorption of the produced inorganic arsenic by a combination of  
979 Co<sub>3</sub>O<sub>4</sub>-La<sub>2</sub>CO<sub>5</sub>@RSBC with peroxymonosulfate, *Chem. Eng. J.* 413 (2021) 127417.  
980 <https://doi.org/https://doi.org/10.1016/j.cej.2020.127417>.
- 981 [68] S. Dong, Q. Ji, Y. Wang, H. Liu, J. Qu, Enhanced phosphate removal using zirconium  
982 hydroxide encapsulated in quaternized cellulose, *J. Environ. Sci.* 89 (2020) 102–112.  
983 <https://doi.org/https://doi.org/10.1016/j.jes.2019.10.005>.
- 984 [69] S. Yang, Y. Liu, Y. Hao, X. Yang, W.A. Goddard III, X.L. Zhang, B. Cao, Oxygen-Vacancy  
985 Abundant Ultrafine Co<sub>3</sub>O<sub>4</sub>/Graphene Composites for High-Rate Supercapacitor Electrodes,  
986 *Adv. Sci.* 5 (2018) 1700659. <https://doi.org/10.1002/advs.201700659>.
- 987 [70] T.L. Phan, L. V Bau, N. V Khiem, N.X. Phuc, S.C. Yu, ESR study of Sr-doped LaCoO<sub>3</sub>  
988 cobaltites, *Phys. Status Solidi.* 242 (2005) 1522–1527.  
989 <https://doi.org/https://doi.org/10.1002/pssb.200440033>.
- 990 [71] C. Sanchez, B. Lebeau, F. Chaput, J.-P. Boilot, Optical Properties of Functional Hybrid  
991 Organic–Inorganic Nanocomposites, *Adv. Mater.* 15 (2003) 1969–1994.  
992 <https://doi.org/10.1002/adma.200300389>.

- 993 [72] A.M. Salih, M. Bin Ahmad, N.A. Ibrahim, K.Z.H.M. Dahlan, R. Tajau, M.H. Mahmood,  
994 W.M.Z.W. Yunus, Synthesis of Radiation Curable Palm Oil-Based Epoxy Acrylate: NMR and  
995 FTIR Spectroscopic Investigations., *Molecules*. 20 (2015) 14191–14211.  
996 <https://doi.org/10.3390/molecules200814191>.
- 997 [73] C. Berthomieu, R. Hienerwadel, Fourier transform infrared (FTIR) spectroscopy, *Photosynth.*  
998 *Res.* 101 (2009) 157–170. <https://doi.org/10.1007/s11120-009-9439-x>.
- 999 [74] G. Zhou, D.-W. Wang, L.-C. Yin, N. Li, F. Li, H.-M. Cheng, Oxygen Bridges between NiO  
1000 Nanosheets and Graphene for Improvement of Lithium Storage, *ACS Nano*. 6 (2012) 3214–  
1001 3223. <https://doi.org/10.1021/nn300098m>.
- 1002 [75] B. Apicella, M. Alfè, R. Barbella, A. Tregrossi, A. Ciajolo, Aromatic structures of  
1003 carbonaceous materials and soot inferred by spectroscopic analysis, *Carbon N. Y.* 42 (2004)  
1004 1583–1589. <https://doi.org/https://doi.org/10.1016/j.carbon.2004.02.010>.
- 1005 [76] V. Țucureanu, A. Matei, A.M. Avram, FTIR Spectroscopy for Carbon Family Study, *Crit. Rev.*  
1006 *Anal. Chem.* 46 (2016) 502–520. <https://doi.org/10.1080/10408347.2016.1157013>.
- 1007 [77] S. Abbott, C.M. Hansen, H. Yamamoto, Hansen solubility parameters in practice complete  
1008 with eBook , software and data, 2013.
- 1009 [78] T. Vasiljevic, T. Harner, Bisphenol A and its analogues in outdoor and indoor air: Properties,  
1010 sources and global levels, *Sci. Total Environ.* 789 (2021) 148013.  
1011 <https://doi.org/https://doi.org/10.1016/j.scitotenv.2021.148013>.
- 1012 [79] S. Sharma, S. Basu, N.P. Shetti, M.N. Nadagouda, T.M. Aminabhavi, Microplastics in the  
1013 environment: Occurrence, perils, and eradication, *Chem. Eng. J.* 408 (2021) 127317.  
1014 <https://doi.org/https://doi.org/10.1016/j.cej.2020.127317>.
- 1015 [80] F. Shoushtarian, M. Negahban-Azar, Worldwide Regulations and Guidelines for Agricultural  
1016 Water Reuse: A Critical Review, *Water*. 12 (2020). <https://doi.org/10.3390/w12040971>.
- 1017 [81] W. Ma, N. Wang, Y. Du, T. Tong, L. Zhang, K.-Y. Andrew Lin, X. Han, One-step synthesis of



- 1018 novel Fe<sub>3</sub>C@nitrogen-doped carbon nanotubes/graphene nanosheets for catalytic degradation  
1019 of Bisphenol A in the presence of peroxymonosulfate, *Chem. Eng. J.* 356 (2019) 1022–1031.  
1020 <https://doi.org/https://doi.org/10.1016/j.cej.2018.09.093>.
- 1021 [82] Y. Liu, R. Luo, Y. Li, J. Qi, C. Wang, J. Li, X. Sun, L. Wang, Sandwich-like Co<sub>3</sub>O<sub>4</sub>/MXene  
1022 composite with enhanced catalytic performance for Bisphenol A degradation, *Chem. Eng. J.*  
1023 347 (2018) 731–740. <https://doi.org/https://doi.org/10.1016/j.cej.2018.04.155>.
- 1024 [83] C. Zhu, F. Liu, C. Ling, H. Jiang, H. Wu, A. Li, Growth of graphene-supported hollow cobalt  
1025 sulfide nanocrystals via MOF-templated ligand exchange as surface-bound radical sinks for  
1026 highly efficient bisphenol A degradation, *Appl. Catal. B Environ.* 242 (2019) 238–248.  
1027 <https://doi.org/https://doi.org/10.1016/j.apcatb.2018.09.088>.
- 1028 [84] X. Li, A.I. Rykov, B. Zhang, Y. Zhang, J. Wang, Graphene encapsulated Fe<sub>x</sub>Co<sub>y</sub> nanocages  
1029 derived from metal–organic frameworks as efficient activators for peroxymonosulfate, *Catal.*  
1030 *Sci. Technol.* 6 (2016) 7486–7494. <https://doi.org/10.1039/C6CY01479H>.
- 1031 [85] C. Wang, H. Wang, R. Luo, C. Liu, J. Li, X. Sun, J. Shen, W. Han, L. Wang, Metal-organic  
1032 framework one-dimensional fibers as efficient catalysts for activating peroxymonosulfate,  
1033 *Chem. Eng. J.* 330 (2017) 262–271. <https://doi.org/https://doi.org/10.1016/j.cej.2017.07.156>.
- 1034 [86] J. Jing, C. Cao, S. Ma, Z. Li, G. Qu, B. Xie, W. Jin, Y. Zhao, Enhanced defect oxygen of  
1035 LaFeO<sub>3</sub>/GO hybrids in promoting persulfate activation for selective and efficient elimination  
1036 of bisphenol A in food wastewater, *Chem. Eng. J.* 407 (2021) 126890.  
1037 <https://doi.org/https://doi.org/10.1016/j.cej.2020.126890>.
- 1038 [87] R. Luo, C. Liu, J. Li, C. Wang, X. Sun, J. Shen, W. Han, L. Wang, Convenient synthesis and  
1039 engineering of ultrafine Co<sub>3</sub>O<sub>4</sub>-incorporated carbon composite: towards practical application  
1040 of environmental remediation, *J. Mater. Chem. A.* 6 (2018) 3454–3461.  
1041 <https://doi.org/10.1039/C7TA11052A>.
- 1042 [88] G.P. Anipsitakis, D.D. Dionysiou, Degradation of Organic Contaminants in Water with Sulfate  
1043 Radicals Generated by the Conjunction of Peroxymonosulfate with Cobalt, *Environ. Sci.*

- 1044 Technol. 37 (2003) 4790–4797. <https://doi.org/10.1021/es0263792>.
- 1045 [89] R. Luo, M. Li, C. Wang, M. Zhang, M.A. Nasir Khan, X. Sun, J. Shen, W. Han, L. Wang, J. Li,  
1046 Singlet oxygen-dominated non-radical oxidation process for efficient degradation of bisphenol  
1047 A under high salinity condition, *Water Res.* 148 (2019) 416–424.  
1048 <https://doi.org/https://doi.org/10.1016/j.watres.2018.10.087>.
- 1049 [90] X. Zhou, C. Luo, M. Luo, Q. Wang, J. Wang, Z. Liao, Z. Chen, Z. Chen, Understanding the  
1050 synergetic effect from foreign metals in bimetallic oxides for PMS activation: A common  
1051 strategy to increase the stoichiometric efficiency of oxidants, *Chem. Eng. J.* 381 (2020)  
1052 122587. <https://doi.org/https://doi.org/10.1016/j.cej.2019.122587>.
- 1053 [91] C. Tan, X. Jian, L. Su, X. Lu, J. Huang, J. Deng, W. Chu, Kinetic removal of acetaminophen  
1054 and phenacetin during LED-UV365 photolysis of persulfate system: Reactive oxygen species  
1055 generation, *Chemosphere.* 269 (2021) 129337.  
1056 <https://doi.org/https://doi.org/10.1016/j.chemosphere.2020.129337>.
- 1057 [92] C. Chen, F. Li, H.-L. Chen, M.G. Kong, Interaction between air plasma-produced aqueous  $^{1}O_2$   
1058 and the spin trap DMPO in electron spin resonance, *Phys. Plasmas.* 24 (2017) 103501.  
1059 <https://doi.org/10.1063/1.4986008>.
- 1060 [93] X. Peng, J. Wu, Z. Zhao, X. Wang, H. Dai, Y. Wei, G. Xu, F. Hu, Activation of  
1061 peroxymonosulfate by single atom Co-N-C catalysts for high-efficient removal of chloroquine  
1062 phosphate via non-radical pathways: Electron-transfer mechanism, *Chem. Eng. J.* 429 (2022)  
1063 132245. <https://doi.org/https://doi.org/10.1016/j.cej.2021.132245>.
- 1064 [94] X. Tian, P. Gao, Y. Nie, C. Yang, Z. Zhou, Y. Li, Y. Wang, A novel singlet oxygen involved  
1065 peroxymonosulfate activation mechanism for degradation of ofloxacin and phenol in water,  
1066 *Chem. Commun.* 53 (2017) 6589–6592. <https://doi.org/10.1039/C7CC02820B>.
- 1067 [95] T. Zhang, Y. Ding, H. Tang, Generation of singlet oxygen over Bi(V)/Bi(III) composite and its  
1068 use for oxidative degradation of organic pollutants, *Chem. Eng. J.* 264 (2015) 681–689.  
1069 <https://doi.org/https://doi.org/10.1016/j.cej.2014.12.014>.

- 1070 [96] E.-T. Yun, J.H. Lee, J. Kim, H.-D. Park, J. Lee, Identifying the Nonradical Mechanism in the  
1071 Peroxymonosulfate Activation Process: Singlet Oxygenation Versus Mediated Electron  
1072 Transfer, *Environ. Sci. Technol.* 52 (2018) 7032–7042.  
1073 <https://doi.org/10.1021/acs.est.8b00959>.
- 1074 [97] Q. Wang, Y. Shao, N. Gao, W. Chu, J. Chen, X. Lu, Y. Zhu, N. An, Activation of  
1075 peroxymonosulfate by Al<sub>2</sub>O<sub>3</sub>-based CoFe<sub>2</sub>O<sub>4</sub> for the degradation of sulfachloropyridazine  
1076 sodium: Kinetics and mechanism, *Sep. Purif. Technol.* 189 (2017) 176–185.  
1077 <https://doi.org/https://doi.org/10.1016/j.seppur.2017.07.046>.
- 1078 [98] Y. Yao, Z. Yang, H. Sun, S. Wang, Hydrothermal Synthesis of Co<sub>3</sub>O<sub>4</sub>–Graphene for  
1079 Heterogeneous Activation of Peroxymonosulfate for Decomposition of Phenol, *Ind. Eng.*  
1080 *Chem. Res.* 51 (2012) 14958–14965. <https://doi.org/10.1021/ie301642g>.
- 1081 [99] Y. Yao, Y. Cai, F. Lu, F. Wei, X. Wang, S. Wang, Magnetic recoverable MnFe<sub>2</sub>O<sub>4</sub> and  
1082 MnFe<sub>2</sub>O<sub>4</sub>-graphene hybrid as heterogeneous catalysts of peroxymonosulfate activation for  
1083 efficient degradation of aqueous organic pollutants, *J. Hazard. Mater.* 270 (2014) 61–70.  
1084 <https://doi.org/https://doi.org/10.1016/j.jhazmat.2014.01.027>.
- 1085 [100] H. V Lutze, N. Kerlin, T.C. Schmidt, Sulfate radical-based water treatment in presence of  
1086 chloride: Formation of chlorate, inter-conversion of sulfate radicals into hydroxyl radicals and  
1087 influence of bicarbonate, *Water Res.* 72 (2015) 349–360.  
1088 <https://doi.org/https://doi.org/10.1016/j.watres.2014.10.006>.
- 1089 [101] W. Duan, J. He, Z. Wei, Z. Dai, C. Feng, A unique Si-doped carbon nanocatalyst for  
1090 peroxymonosulfate (PMS) activation: insights into the singlet oxygen generation mechanism  
1091 and the abnormal salt effect, *Environ. Sci. Nano.* 7 (2020) 2982–2994.  
1092 <https://doi.org/10.1039/D0EN00848F>.
- 1093 [102] A. Shahzad, J. Ali, J. Ifthikar, G.G. Aregay, J. Zhu, Z. Chen, Z. Chen, Non-radical PMS  
1094 activation by the nanohybrid material with periodic confinement of reduced graphene oxide  
1095 (rGO) and Cu hydroxides, *J. Hazard. Mater.* 392 (2020) 122316.

1096 <https://doi.org/https://doi.org/10.1016/j.jhazmat.2020.122316>.

1097 [103] S. Yang, P. Wu, J. Liu, M. Chen, Z. Ahmed, N. Zhu, Efficient removal of bisphenol A by  
1098 superoxide radical and singlet oxygen generated from peroxymonosulfate activated with FeO-  
1099 montmorillonite, Chem. Eng. J. 350 (2018) 484–495.

1100 <https://doi.org/https://doi.org/10.1016/j.cej.2018.04.175>.

1101 [104] S. Wang, J. Tian, Q. Wang, F. Xiao, S. Gao, W. Shi, F. Cui, Development of CuO coated  
1102 ceramic hollow fiber membrane for peroxymonosulfate activation: a highly efficient singlet  
1103 oxygen-dominated oxidation process for bisphenol a degradation, Appl. Catal. B Environ. 256  
1104 (2019) 117783. <https://doi.org/https://doi.org/10.1016/j.apcatb.2019.117783>.

1105

1106

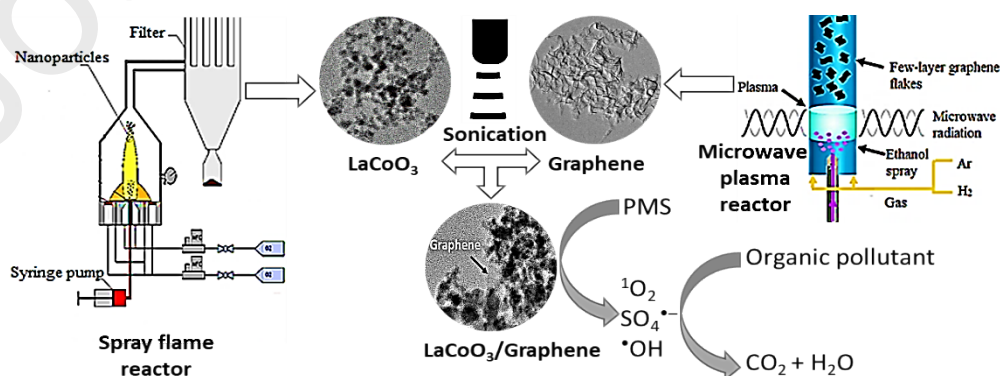
1107

1108 Graphical abstract

## 1109 Synthesis of novel $\text{LaCoO}_3$ /graphene catalysts as highly efficient 1110 peroxymonosulfate activator for the degradation of organic pollutants

1111 Mohaned Hammad<sup>a\*</sup>, Steven Angel<sup>c</sup>, Ahmed K. Al-kamal<sup>c,g</sup>, Anam Asghar<sup>b</sup>, Amin Said Amin<sup>a</sup>,  
1112 Haakon T. A. Wiedemann<sup>d</sup>, Md Yusuf Ali<sup>c</sup>, Paolo Fortugno<sup>c</sup>, Cheolyong Kim<sup>b</sup>, Torsten C.  
1113 Schmidt<sup>b</sup>, Christopher W. M. Kay<sup>d,f</sup>, Doris Segets<sup>a,e</sup>, Hartmut Wiggers<sup>c,e\*</sup>

1114



1115

1116

1117

1118

1119 **Highlight**

- 1120 • Large-scale synthesis of novel LaCoO<sub>3</sub>/Graphene material is presented.
- 1121 • LaCoO<sub>3</sub>/Graphene composite exhibits outstanding PMS activation efficiency than LaCoO<sub>3</sub>.
- 1122 • Co–O–C interactions improve the stability and prevent cobalt leaching.
- 1123 • LaCoO<sub>3</sub>/Graphene material has an excellent performance under various environmental
- 1124 factors.

1125

1126